frontiers | Frontiers in Earth Science

TYPE Original Research
PUBLISHED 06 January 2025
DOI 10.3389/feart.2024.1497913

OPEN ACCESS

EDITED BY
Wei-Qiang Ji,
Chinese Academy of Sciences (CAS), China

REVIEWED BY
Yu Li,
Institute of Geology and Geophysics (CAS), China
Zheng Liu,
Yunnan University, China

*CORRESPONDENCE
Jing Sun,
sunjingvv@163.com

†These authors have contributed equally to this work

RECEIVED 18 September 2024
ACCEPTED 30 October 2024
PUBLISHED 06 January 2025

CITATION
He W, Wang H, Su J, Wang W, Zhao J, Zuo G, Wang T, Yang L, Ren K, Wang C, Zhao J, Guo Y, Zhang Y and Sun J (2025) Magma evolution during the post-rift phase of the Santos Basin, Brazil: petrogenesis and geochemistry of ~126–121 ma basalts and diabases.
Front. Earth Sci. 12:1497913.
doi: 10.3389/feart.2024.1497913

Magma evolution during the post-rift phase of the Santos Basin, Brazil: petrogenesis and geochemistry of ~126–121 ma basalts and diabases

Wenyuan He[1†], Hongping Wang[2†], Jinglin Su[3], Wangquan Wang[1], Junfeng Zhao[4], Guoping Zuo[2], Tongkui Wang[4], Liu Yang[2], Kangxu Ren[4], Chaofeng Wang[2], Jian Zhao[4], Yuan Guo[4], Yonggang Zhang[2] and Jing Sun[3]*

[1]China National Oil and Gas Exploration and Development Corporation, Beijing, China, [2]PetroChina Hangzhou Research Institute of Geology, Hangzhou, China, [3]College of Geosciences, China University of Petroleum, Beijing, China, [4]CNPC Brasil Petroleo e Gas Ltda, Rio deJaneiro, Brazil

The Santos Basin, a passive continental margin basin recognized for its vast deep-sea hydrocarbon potential, poses unique geological issues due to the large amount of igneous rocks revealed by drilling data. In order to understand the magmatic evolution during the post-rift phase, we studied petrology, major elements, trace elements, and Sr-Nd isotopic composition of bulk rock, and Ar-Ar dating on whole rock and minerals on basalts and diabases from Santos Basin. Ar-Ar dating results suggest that basalts and diabases emplaced on ~126–121 Ma. The geochemistry and Sr-Nd isotopic compositions indicates the derivation of these rocks from the spinel and garnet lherzolite facies, denoted by increased La/Sm ratios that suggest a 1%–5% degree of partial melting. These findings correspond with the characteristics of continental rift basalts. The geochemical analysis hints that the older basalts and diabases were likely derived from the asthenospheric mantle, whereas the younger ones display a geochemical mix indicative of contributions from both the deeper asthenosphere and the subcontinental lithospheric mantle (SCLM), or possibly from crustal contamination. A proposed hypothetical model indicating that the deepening of the basin into the asthenosphere, in conjunction with the thinning and stretching of the lithosphere, could have been instrumental in the magmatic events recorded in the region.

KEYWORDS

santos basin, pre-salt, continental rift basalts, Sr-Nd isotopes, Ar-Ar dating

1 Introduction

The tectonic model is crucial for understanding rift-related sedimentary oil and gas basins. Most of these models are primarily constrained by geophysics and seismic surveys, whereas the mantle dynamics and magmatic process during basin evolution are little known (Zalán et al., 2011; Stanton et al., 2014; Evain et al., 2015). It is important to determine the time and duration of the magmatic events to evaluate the effects of intrusions and

volcanism in petroleum systems of a sedimentary basin, as magmatism in a sedimentary basin may induce thermal and fluid gradients, which in turn affect the properties of source and reservoir rocks (Filho et al., 2000; Gudmundsson and Lotvei, 2014; Senger et al., 2017; Wu et al., 2021).

Santos Basin, situated along the southeastern coast of Brazil, is a passive continental margin basin. It contains billions of barrels of unexplored oil and gas resources in many blocks, with Libra block currently regarded as one of the world's biggest Pre-Salt oil fields. Most importantly, the Santos Basin contains considerable amounts of multiple episodes of igneous rocks, making it an ideal place to understand the basin's tectonic evolution via magmatic activities. Formed as a fragmentation of Gondwana in the Early Cretaceous, it then evolved into a passive margin basin due to the opening of the South Atlantic Ocean (Chang et al., 1992; Cainelli and Mohriak, 1999). Having its formation during the breakup of Gondwana, and as part of the larger tectonic event that created a series of rift basins along both sides of the South Atlantic, the basin has undergone multiple phases of rifting and post-rifting, resulting in the deposition of thick sequences of sedimentary rocks and igneous rocks. Due to the thick sedimentary salt layers and pre-salt reservoirs, the Santos Basin has attracted significant attention because of its complex geological history and vast potential hydrocarbon reserves (Bruhn et al., 2017).

Previous geophysical and tectonic-structural studies have provided a detailed understanding of the rifting architecture and evolution of the Santos Basin, revealing a crystalline basement composed of Ribeira Belt rocks shaped by ancient orogenic events (Heilbron et al., 2008). Influenced by mantle activity and oblique extension of the northern basin, the basin's tectonic stages, from pre-rift to drift, showcase a transition from continental to oceanic structures. As the Outer High encompass a complicated uplift and erosion history, and based on seismic insights into the Tupi oil field, the role of salt tectonics in shaping the basin's structural framework are crucial for hydrocarbon exploration. Also, the magmatic processes are associated with the rift, post-rift, and drift sedimentary mega-sequences recorded in the chronostratigraphic column of the basin (Fodor and Vetter, 1984; Moreira et al., 2006; Moreira et al., 2007). The rift-related magmatism (138 Ma, whole rock K-Ar ages of Camboriu basalt; Fodor and Vetter, 1984) in Santos was almost coeval with the Parana-Etendeka CFB main magmatism (134.7 Ma, Ar-Ar ages; Thiede and Vasconcelos, 2010). The post-rift stage spanned from ca. 123 Ma to ca. 112 Ma (Aptain), including several sequences known as the Barra Velha and Ariri formations (Gordon et al., 2023). If combining formation mechanism affected by Gondwana breakup and South Atlantic opening with geochemical evidences, the Santos Basin will offer valuable insights when compared with other Brazilian and African basins (Stanton et al., 2014; Ren et al., 2020; Adriano et al., 2022; Marins et al., 2022).

However, the petrogenesis and geochemistry of Santos Basin's igneous rocks remain poorly understood. Most studies on magmatism in Santos focus primarily on the pre-rift and rifting processes, with post-rift magmatism rarely systematically studied. Such a gap limits the understanding of magma evolution and tectonic activity after rifting. In this study, by examining the ~126–121 Ma basalts and diabases of the post-rift stage, we provide petrographic, geochemistry, Sr-Nd isotope and Ar-Ar geochronological data for the post-rift extrusive basalts and intrusive diabases in the pre-salt sedimentary of Santos basin to fill this gap, providing insights into the magmatic and tectonic evolution of the basin. In addition, previously studied post-rift basalts from Santos Basin were used to discuss the magma evolution and geodynamic model during the post-rift process in Santos Basin.

2 Geological background and sample descriptions

2.1 Geological background

West Gondwana represents Precambrian shields in South America (Figure 1A; Almeida et al., 1981). It consists of Paleo-Neoarchean (3.6–2.7 Ga) terranes reworked during Paleo-to Neoproterozoic collisional orogenies (e.g., Dantas et al., 2004; Ganade de Araujo et al., 2014). The Archean crustal fragments can be considered as small Archean cores surrounded by Paleo- to Neoproterozoic granite-gneiss terranes and supracrustal sequences (e.g., Brito Neves and Fuck, 2014). The disassembly of Gondwana began approximately 135 Ma ago in southeastern Brazil, marked by the initial manifestations of lithospheric stretching during the pre-rift phase. This process produced a large-scale fractured crustal framework without significant crustal thinning, the extrusion of large continental flood basalts and the formation of dike swarms (Heilbron et al., 2000; Mohriak and Rosendahl, 2003; Almeida et al., 2013).

The Santos Basin is a sedimentary basin on the passive margin, located offshore along the southeastern continental margin of Brazil, near the state coastlines of Rio de Janeiro, Sao Paulo, Parana, and Santa Catarina (Figure 1B). The basin covers an area of approximately 350,000 km^2, bounded to the north by the Cabo Frio Structural High and to the south by the Florianópolis Structural High. The Santos Basin is further divided into Sao Sebastiao High and Sao Paulo Plateau. Located in the Sao Paulo Plateau, Block L, is approximately 200 km off the coast of Rio de Janeiro, Brazil, containing some of the largest ultra-deepwater pre-salt oilfields (Wang et al., 2019). Also located in the Santos Basin, Block BM S11, its reservoir stands at a water depth of around 3,500 m. The thickness of overlaying Salt Cap Rock varies from several hundred meters to 2000 m (Wang et al., 2019). The primary reservoirs are lacustrine carbonates, deposited from the Neobarremian until the Aptian (Carlotto et al., 2017). The field is estimated to contain billions barrels of oil, with Petrobras estimating its overall recoverable volume at 3.3 billion barrels of oil. Santos Basin comprises one of the thickest sedimentary sequences (~10 km) among the basins of the Brazilian continental margin. The chronostratigraphic chart of Santos Basin comprises three major sedimentary sequences related to the Gondwana rifting processes and the further development of the South Atlantic Ocean (Moreira et al., 2007). The geological evolution of the Santos Basin can be divided into three phases (Rift, Post-Rift, and Drift), each of them correlated to the records of sedimentary mega-sequences and magmatic events (Gordon et al., 2023). The rift sequence captures the sedimentation over a thinned and extensively stretched crust, with half-grabens filled by the tholeiitic basalts of the Camboriu Formation at their lowermost

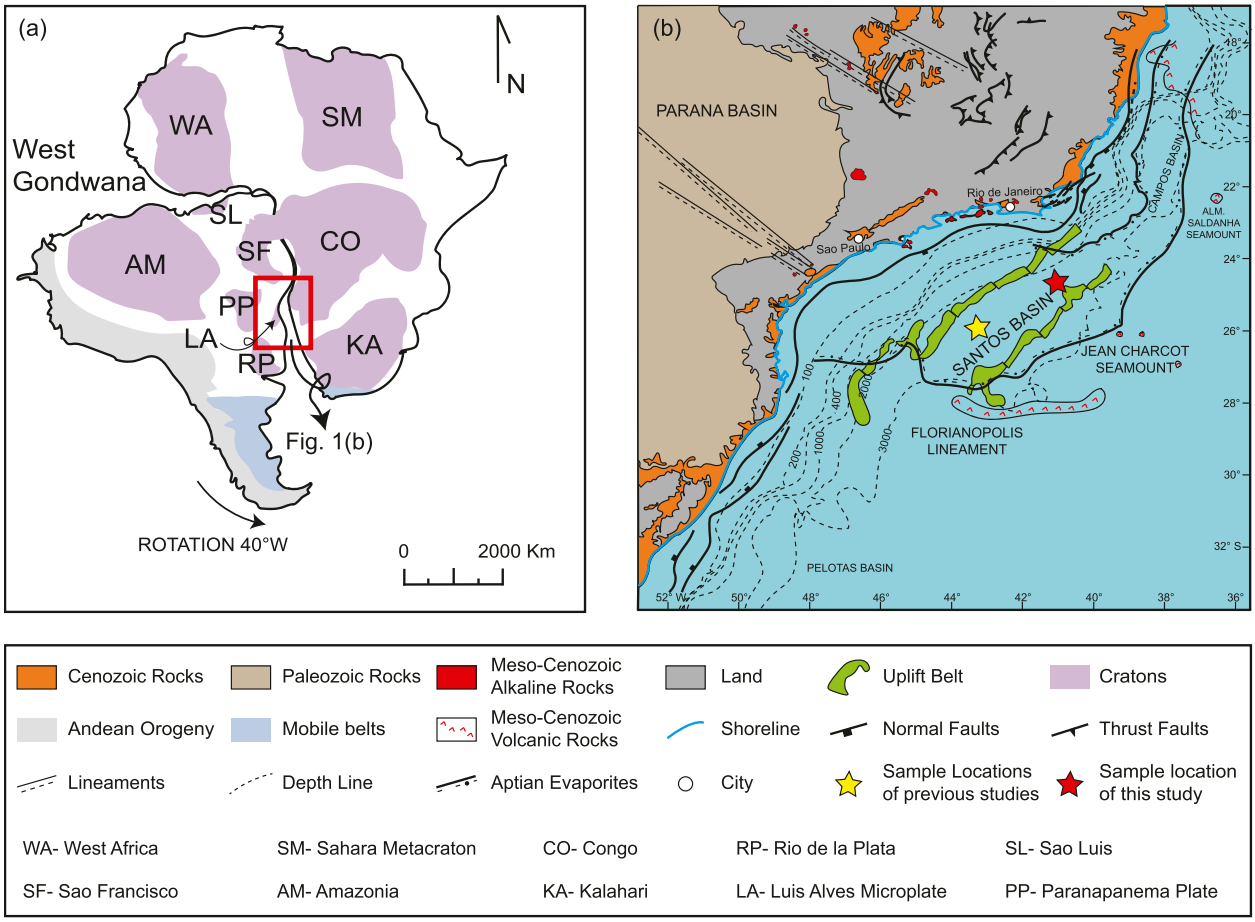

FIGURE 1
Paleoreconstruction of west Gondwana modified from Almeida et al. (2021) **(A)** and the location of the Santos Basin in Southeast Brazil **(B)**. In Figure 1A, The South American continent has been rotated 40°W to its pre-break-up position whilst the American continent remains fixed. The Figure 1A is modified from Mohriak et al. (1995).

sections (Mio et al., 2005; Chang et al., 2008). The Rift Sequence concludes with the deposition of the coquinas and dark shales from the Itapema Formation over an Intra-Barremian unconformity. Hydrocarbon source and reservoir rocks in the Pre-Salt sedimentary sequence of Santos Basin are found in the Picarras and Itapema formations respectively, forming part of one of the world's most significant petroleum systems (Zalán and Newman, 2019). The post-rift sequence in Santos Basin preserves predominantly evaporitic cycles typical of shallow water lacustrine depositional condition (Wright and Rodriguez, 2018), which constitutes the seal rocks of the Pre-Salt petroleum systems within Santos Basin (Moreira et al., 2007). The drift sequence is related to the increasing thermal subsidence of the basin, resulting in the deposition of marine sediments from the Albian to the Recent. Subsequently, the shallow marine carbonate platform resulted from the rising sea level covered the Aptian evaporite (Chang et al., 1992).

The drilling results reveal igneous rocks' presence at in-salt, post-salt, and primarily pre-salt locations, in Picarras, Itapema, and Barra Velha Formation (Figure 2). Pre-salt reservoir types such as diapiric anticline, faulted anticline, and other types are intimately associated with volcanism. In recent years, oil and gas reservoirs related to igneous rocks have drawn increasing interest, and the exploration focus has expanded. The Block L offers valuable drilling, seismic, logging, geochronological, and geochemical information on igneous rocks. Further research will not only aid exploration efforts but also provide new insights into the tectonic evolution of Santos Basin.

2.2 Sample description

In this study, certain well names and depth data have been concealed (such as: Well Y and X184 m) following specific confidentiality agreements with oil company. We assure that throughout the process of data collection, analysis, and interpretation, we have adhered to the principles of scientific rigor and have endeavored to ensure the accuracy and reliability of the results.

The drilling results indicate several cross-cuts of igneous rocks. From X184- X475.8 m, a large amount of basalt is cut by two separated diabase intervals, with sedimentary layers in between. From X529.2-X704.0 m, basalt is cut by a thin interval of diabase, also interbedded with several limestone layers. From X704-X805 m, thick diabase is emplaced above the 2 intervals of basalts which are interbedded with limestone and mudstone.

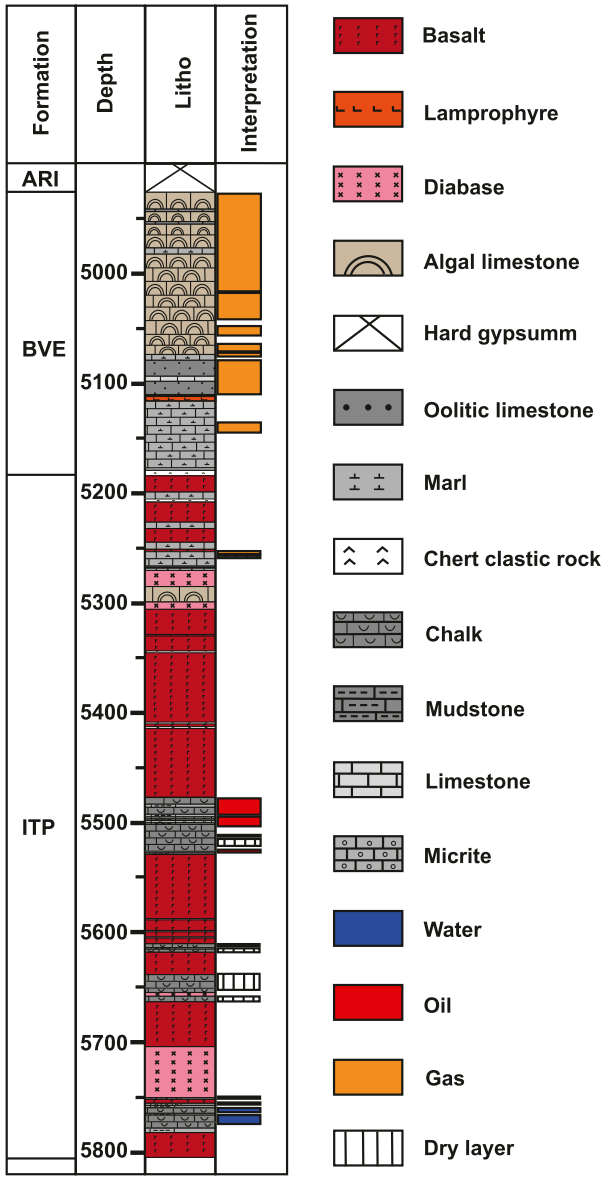

FIGURE 2
Simplified composite log of the pre-salt section of borehole Well Y.

Seventy-five Sidewall cores of igneous rocks from Well Y and its side track were sampled, with forty-three sent for geochemical analysis, and ten analyzed for Sr-Nd isotopic data. The igneous samples include both intrusive and extrusive facies, such as diabase, hyaloclastite, and basalts. Diabases in this study with diabasic texture contain lower glassy content, and their euhedral plagioclases always form triangular structures and anhedral augites fill in between. As intrusive facies, diabase is a fine-to medium-grained rock with variable phenocryst amounts and textures, including plagioclase, rare olivine, and pyroxene (Figure 3A). They underwent minor alteration, and fractures are filled with carbonate, replacing pyroxene and part of the plagioclase. Such alteration and minerals replaced by carbonate are quite usual for underwater drilling core samples, especially when interbed with sedimentary carbonate strata. Extrusive basalts are further divided into massive basalt and amygdaloidal basalt. It should be noted that the well Y contains a mass of basalts from X180 m to X800 m (Figure 2). The basalts we discussed in this study are those only occurred between diabase intrusions, which is from X300 m to X700 m. The massive basalts (Figure 3B), with 10%–30% volcanic glass, show diverse textures and contain phenocrysts (altered plagioclase, rare olivine) with secondary minerals (carbonate, sericite, albite, sulfide, zeolite). The groundmass has quench plagioclase, augite, volcanic glass, and opaque minerals. Samples with higher glass ratios and sharp contacts indicate faster cooling. Amygdaloidal basalt (Figure 3C) with 5%–30% volcanic glass, has 5%–25% amygdale concentration (0.5–10 mm) and variable texture. Phenocrysts include plagioclase, and rare olivine; groundmass are plagioclase, and pyroxene. The absence of pyroxene implies rapid cooling. Significant alteration and secondary minerals (carbonate, clay, zeolite, sulfide) replacing essential minerals and volcanic glass are observed. Examples of hyaloclastite at X180.0 m, X408.8 m, X201 m, X413.2 m, X329.1 m, X537.1 m, X343.9 m. Underwater-erupted hyaloclastite (Figure 3D) consists of glassy basalt fragments cemented by minerals, primarily plagioclase, with secondary sulfide, Mg-rich clay, carbonate, and zeolite. Amygdales (1–2.5 mm) and fractures are commonly filled with these minerals.

3 Analytical method

3.1 Major and trace elements

Thin sections were investigated under an optical microscope Zeiss AxioVision with transmitted light, at CENPES. For the petrographic description and classification, it is applied Le Maitre´s nomenclature recommended by IUGS–International Union of Geological Sciences Subcommission on the Systematics of Igneous Rocks (Streckeisen, 1978; Le Maitre et al., 2002). The major and trace elements of whole rocks were analyzed at Activation Laboratories Ltd. (Actlabs, Canada). Litho-geochemical analyses consist the measure of concentration of major oxides on ICP-OES (Inductively Coupled Plasma-Optical Emission Spectrometry), whereas selected trace elements (Ni, Cr, Co., Ba, Rb, Sr, Zr, Y, Nb, Ni, Cr, V, Co., U, Th, Hf, Ta and Pb), including the whole set of rare earth elements on ICP-MS (Inductively Coupled Plasma-Mass Spectrometry). The sample is crushed to a nominal minus 10 meshes (1.7 nm), mechanically split to obtain a representative sample, and then pulverized to at least 95% minus 150 meshes (105 microns) in a steel mill. For elements extraction, the prepared sample was mixed well with the lithium metaborate/lithium tetraborate, and heated at 1,000°C. Then the melt was cooled and dissolved by 100 mL of 4% nitric acid/2% hydrochloric acid. The solution was analyzed by ICP-OES. For the trace elements, the prepared sample was dissolved in 100 mL of 4% HNO_3/2% HCl_3 solution. The solution was then analyzed by ICP-MS.

3.2 Sr-Nd isotopic compositions

The isotopic ratios of magma reflect its source's characteristics and remain stable during fractional processes unless contaminated by host rocks or different magmatic pulses

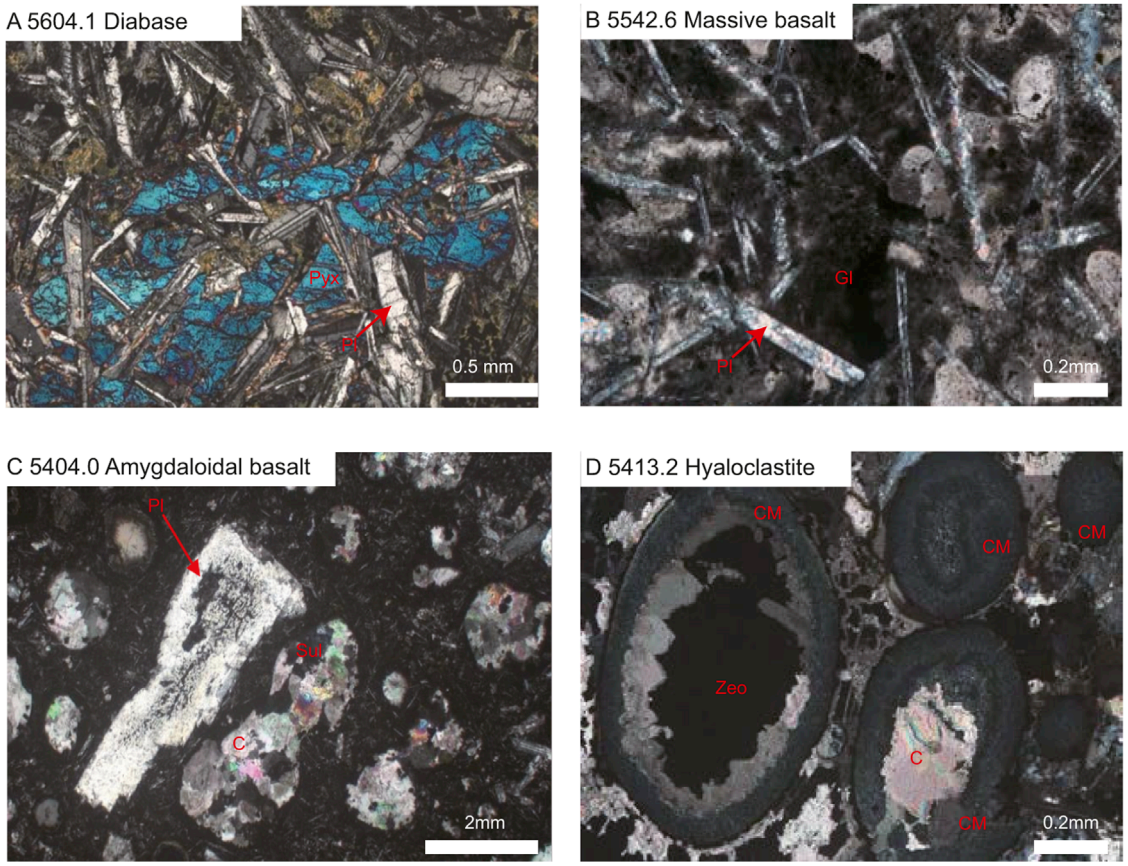

FIGURE 3
Photomicrographs of representative samples of the studied diabase **(A)**, massive basalt **(B)**, amygdaloidal basalt **(C)**, hyaloclastite **(D)**. Pl plagioclase; Pyx pyroxene; Zeo zeolite; Sul sulfide; CM Mg-rich clay mineral; C carbonate.

(Rollinson., 1993; Wilson., 1989). Assimilation of crustal rocks or mixing with other magmas can cause isotopic variations. To avoid post-magmatic alterations, the fresh igneous samples are selected for analysis. Issues such as amygdales, micro fractures, or venules with non-magmatic minerals might affect isotopic ratios. When ideal samples are scarce, such as in sidewall core samples, the degree of alteration (indicated by Loss on Ignition, LOI) and petrographic characteristics are key selection criteria. Out of all sample selected for isotopic analysis, only one diabase (12.51%) and one amygdaloidal basalt (11.74%) sample have LOI higher than 10%. Apart from that, the LOI of other analyzed samples for Sr-Nd isotopes range from 6.22% to 9.8%.

Ten basalt and diabase rock samples underwent isotopic analysis for neodymium (Nd), and strontium (Sr) using multicollector inductively coupled plasma mass spectrometry (MC-ICP-MS) and thermal ionization mass spectrometry (TIMS). The chemical preparation was conducted at the PicoTrace chemistry lab within the Lamont-Doherty Earth Observatory. Approximately 200 mg of each powdered sample were weighed into acid-cleaned Teflon beakers and subjected to leaching with double-distilled 6N HCl on a hotplate at 120°C for 1 hour to remove any seawater contamination, following the leaching methods described by Weis et al. (1991), Weis and Frey (1996). After leaching, the samples were transferred to acid-cleaned centrifuge tubes, centrifuged to remove the leachate, and then dissolved using Optima-grade hydrofluoric acid and double-distilled nitric acid in laminar flow hoods.

Once fully dissolved, the samples were processed through column chromatography according to Cai et al. (2015); Li et al. (2016). The Nd-isotope analysis was conducted on a Nu Instruments Plasma II MC-ICP-MS at the FIRST Stony Brook laboratory, with neodymium values normalized to the JNdi standard ratio of 0.512,115 for $^{143}Nd/^{144}Nd$, following Tanaka et al. (2000). The Sr-isotope analysis was carried out on an Isotopx Phoenix 64 TIMS at the FIRST Stony Brook laboratory, with strontium values monitored against the NIST/NBS SRM 987 standard, using a ratio of 0.710,248 for $^{87}Sr/^{86}Sr$, without normalization.

3.3 Ar-Ar dating

The rock samples were meticulously prepared for isotopic analysis through a series of cleaning and treatment steps. Initially, they were hand-crushed to a size of minus 2 mm and then washed in an ultrasonic bath with water to remove fine particles. Following this, the samples were treated with 3.5N HCl for 1 hour and subsequently washed twice with distilled water in an ultrasonic bath. They were then treated with N HNO_3 for another hour and washed twice more with distilled water. After this, the samples were cleaned

TABLE 1 Whole rock major element compositions of samples of borehole Well Y in Santos Basin.

Petrology	Depth	SiO_2	TiO_2	Al_2O_3	Fe_2O_3(T)	MnO	MgO	CaO	Na_2O	K_2O	P_2O_5	LOI	Total
Massive basalt	5,451.20	42.42	1.647	13.72	6.91	0.134	6.1	10.48	2.24	4.13	0.19	12.72	100.7
Massive basalt	5,455.90	46.17	1.686	16.6	7.11	0.095	5.04	7.18	3.17	3.97	0.18	9.15	100.4
Massive basalt	5,466.60	44.86	1.572	14.63	7.27	0.115	5.88	7.31	3.87	3.8	0.19	10.84	100.3
Massive basalt	5,469.30	39.66	1.686	12.97	6.55	0.047	2.71	14.81	3.58	4.31	0.28	11.82	98.43
Massive basalt	5,540.80	41.82	1.247	14.82	7.67	0.138	4.55	12.17	2.08	3.68	0.22	10.52	98.9
Massive basalt	5,553.50	48.94	1.463	15.26	7.38	0.104	5.99	7.19	4.28	2.9	0.16	6.65	100.3
Massive basalt	5,565.30	44.73	1.392	15.34	8.5	0.144	6.72	8.03	4.18	1.93	0.22	9.43	100.6
Massive basalt	5,628.60	43.32	1.76	13.52	7.33	0.076	3.29	6.95	1.66	7.15	0.26	13.73	99.05
Massive basalt	5,679.30	46.22	1.719	15.31	6.93	0.06	4.97	5.14	2.68	6.91	0.23	10.02	100.2
Poorly Amygdaloidal basalt	5,683.10	45.08	1.508	16.48	7.92	0.049	3.97	4.68	6.11	3	0.09	9.61	98.5
Poorly Amygdaloidal basalt	5,689.90	45.61	1.767	15.08	6.43	0.111	4.92	7.83	3.14	4.88	0.24	9.8	99.81
Poorly Amygdaloidal basalt	5,690.20	44.82	1.65	15.68	5.56	0.114	6.74	8.45	3.12	4	0.21	10.26	100.6
Amygdaloidal basalt	5,189.00	43.79	1.508	14.42	6.75	0.111	3.29	11.55	1.65	5.35	0.67	11.14	100.2
Amygdaloidal basalt	5,349.20	41.84	1.485	11.75	7.05	0.154	8.27	9.64	1.96	3.7	0.27	13.83	99.93
Amygdaloidal basalt	5,357.80	39.73	1.639	13.06	6.07	0.146	5.74	17.04	2.45	1.85	0.18	10.96	98.86
Amygdaloidal basalt	5,367.40	42.38	1.567	13.44	5.98	0.14	5.34	12.38	1.67	4.78	0.2	12.29	100.2
Amygdaloidal basalt	5,372.90	40.65	1.537	12.63	5.91	0.151	4.35	15.57	1.9	4.11	0.22	11.79	98.83
Amygdaloidal basalt	5,432.00	46.76	1.67	15.88	7.79	0.061	7.73	3.71	2.9	4.39	0.22	9.17	100.3
Amygdaloidal basalt	5,447.20	46.81	1.877	15.86	7.26	0.093	6.48	5.52	4.58	2.76	0.24	8.81	100.3
Amygdaloidal basalt	5,570.10	44.8	1.295	13.99	5.74	0.091	1.64	11.27	2.25	7.9	0.15	10.25	99.38
Amygdaloidal basalt	5,577.40	45.3	1.401	16.37	5.11	0.124	4.21	14.29	4.26	1.63	0.19	7.77	100.6
Amygdaloidal basalt	5,620.10	47.5	1.65	15.29	7.74	0.058	2.5	5.68	2.83	5.51	0.22	11.74	100.7
Diabase	5,279.60	39.51	0.823	13.79	7.97	0.118	5.2	14.86	2.27	0.43	0.14	14.25	99.35
Diabase	5,283.90	42.3	1.066	16.18	9.01	0.071	5.46	10.4	2.61	0.62	0.1	12.51	100.3
Diabase	5,306.00	43.06	1.087	13.95	8.05	0.148	6.58	12.09	2.63	0.86	0.09	12.11	100.7

(Continued on the following page)

TABLE 1 (*Continued*) Whole rock major element compositions of samples of borehole Well Y in Santos Basin.

Petrology	Depth	SiO_2	TiO_2	Al_2O_3	Fe_2O_3(T)	MnO	MgO	CaO	Na_2O	K_2O	P_2O_5	LOI	Total
Diabase	5,542.60	41.98	1.288	14.69	6.98	0.131	3	12.91	2.98	4.09	0.2	10.33	98.58
Diabase	5,572.70	42.87	1.298	14.93	7.72	0.129	5.36	11.35	3.13	2.8	0.21	10.76	100.6
Diabase	5,587.70	45.97	1.357	16.26	8.05	0.118	8.95	10.07	2.25	0.9	0.15	6.43	100.5
Diabase	5,598.90	36.92	1.214	12.1	7.53	0.2	4.55	19.79	1.95	1.79	0.15	12.51	98.69
Diabase	5,604.10	46.88	1.766	16.81	6.83	0.112	3.82	7.97	4.47	3.72	0.22	8.07	100.7
Diabase	5,635.90	40.8	1.46	14.14	7.65	0.105	4.08	8.78	1.89	5.41	0.24	15.99	100.6
Diabase	5,656.20	45.8	1.652	15.27	7.9	0.086	8.1	6.13	1.84	3.67	0.16	9.6	100.2
Diabase	5,657.10	47.93	1.78	15.97	7.18	0.084	6.8	8.71	2.46	1.73	0.17	6.77	99.59
Diabase	5,658.20	34.22	1.195	11.9	4.34	0.12	2.11	22.82	1.54	4.14	0.14	15.63	98.15
Diabase	5,666.20	44.41	1.436	14.54	12.37	0.038	4.84	3.07	2.24	6.3	0.16	10.91	100.3
Diabase	5,671.30	47.15	1.766	15.12	7.3	0.042	6.9	3.65	2.75	5.59	0.27	9.19	99.72
Diabase	5,675.10	45.69	2.116	15.02	9.45	0.054	5.09	3.04	0.89	8.69	0.25	9.54	99.83
Diabase	5,704.00	44.04	1.985	15.51	6.3	0.148	3.92	15.9	2.81	1.77	0.24	6.87	99.51
Diabase	5,708.80	47.61	1.683	16.15	7.53	0.088	6.03	9.74	3.74	1.79	0.17	6.22	100.8
Diabase	5,716.40	47.8	1.903	15.32	7.74	0.09	5.94	6.7	5.22	1.75	0.21	7.23	99.91
Diabase	5,721.40	46.17	1.521	15.55	8.44	0.102	6.61	8.17	4.47	1.81	0.17	6.94	99.95
Diabase	5,724.80	47.54	1.628	16.38	8.01	0.107	6.43	7.5	4.18	1.98	0.2	6.69	100.6
Diabase	5,735.00	42.87	1.374	14.31	6.83	0.123	6.03	16.34	2.1	1.03	0.13	8.64	99.78

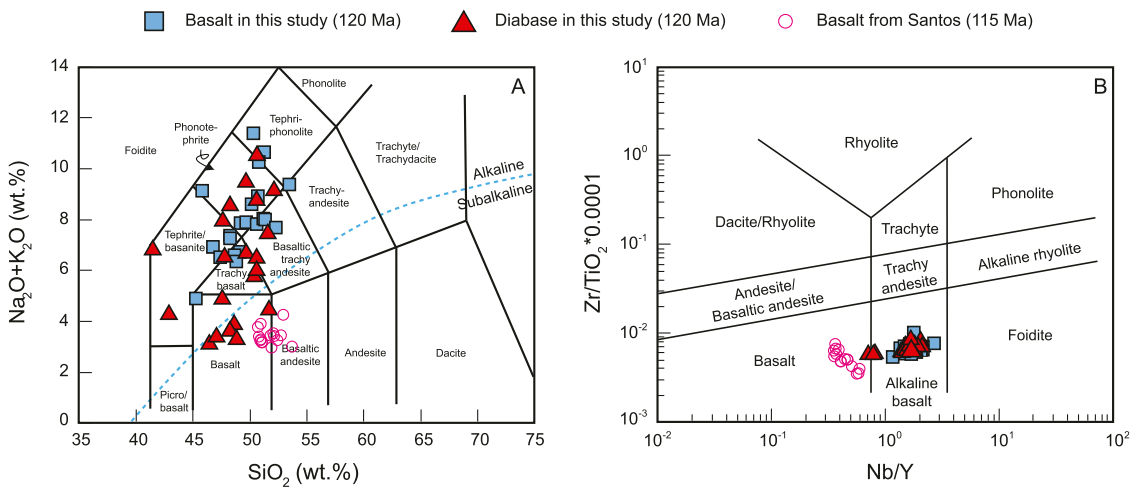

FIGURE 4
Geochemical data of basalts and diabases from borehole Well Y in Santos Basin. Basalts of 115 Ma from Louback et al. (2023) **(A)** samples plotted in the total alkalis vs. SiO_2 (TAS) diagram (in wt%). Classification after Le Bas et al. (1986). **(B)** Zr/TiO_2 vs. Nb/Y diagram (Winchester and Floyd, 1977) for basalts and diabases from borehole Well Y in Santos Basin.

TABLE 2 Whole rock trace element compositions of samples of borehole Well Y in Santos Basin.

Petrology	Depth	Sc	V	Cr	Co.	Ni	Cu	Zn	Ga	Ge	As	Rb	Sr	Ba	Nb	Ta	Zr	Hf	Th	U	La	Ce	Pr	Nd	Sm	Eu	Gd	Tb	Dy	Ho	Er	Tm	Yb	Lu	Y
Ditection limit		1	5	20	1	20	10	30	1	0.5	5	1	2	3	0.2	0.01	1	0.1	0.05	0.01	0.05	0.05	0.01	0.05	0.01	0.005	0.01	0.01	0.01	0.01	0.01	0.005	0.01	0.002	0.5
Massive basalt	5,451.20	29	209	200	25	70	70	<30	13	0.7	34	36	509	481	31.6	3.21	113	3.3	1.4	6.42	12.9	26.3	3.21	13.3	3.24	1.08	3.37	0.58	3.37	0.68	1.96	0.295	1.95	0.3	18.8
Massive basalt	5,455.90	30	221	290	34	130	80	50	15	1	37	42	493	443	32.4	3.32	119	3.3	1.4	3.21	13	26.6	3.38	13.8	3.41	1.21	3.63	0.61	3.67	0.69	2	0.308	1.99	0.297	19.3
Massive basalt	5,466.60	26	197	250	31	110	70	30	12	0.8	58	36	536	846	31	3.06	99	3.1	1.34	5.52	11.8	24.2	3.12	13.1	3.19	1.12	3.47	0.6	3.58	0.67	2.02	0.3	1.85	0.279	18.6
Massive basalt	5,469.30	26	171	130	28	90	90	40	10	0.7	122	50	314	468	35.8	3.12	108	2.5	1.38	3.86	13.6	27.9	3.61	15.5	3.79	1.36	3.64	0.63	3.98	0.77	2.19	0.323	2.18	0.342	21.4
Massive basalt	5,540.80	29	197	260	31	110	80	40	12	0.8	<5	32	510	551	20.6	2.17	67	2.1	1.22	0.72	11.4	22.4	2.87	12.1	2.74	0.997	3.14	0.51	3.06	0.65	1.94	0.277	1.74	0.256	17.7
Massive basalt	5,553.50	32	213	290	38	120	80	50	11	1	<5	27	354	497	26.1	2.42	89	2.5	1.5	0.35	11.9	24.2	3.07	12.5	3.1	1.1	3.26	0.53	3.19	0.62	1.76	0.247	1.55	0.244	16.8
Massive basalt	5,565.30	31	203	340	38	150	90	50	13	0.7	<5	23	534	333	25.5	2.48	94	2.6	1.44	0.39	12.8	25.5	3.23	12.8	3.02	1.07	3.29	0.56	3.51	0.69	2.01	0.299	1.93	0.284	18.8
Massive basalt	5,628.60	26	200	250	35	100	80	<30	12	0.6	13	61	172	734	33.5	3.96	111	3.3	1.69	2.5	14.2	28.6	3.55	14.1	3.34	1.14	3.38	0.55	3.3	0.65	1.83	0.267	1.73	0.261	18.1
Massive basalt	5,679.30	27	206	190	34	90	70	70	12	0.8	<5	86	261	703	36.2	3.52	135	3.5	1.84	0.6	15.4	31.5	4	16.3	3.92	1.23	3.83	0.64	3.79	0.72	2.02	0.295	1.87	0.3	20.1
Poorly Amygdaloidal basalt	5,683.10	22	187	200	38	100	80	160	10	0.7	<5	43	153	356	31.3	2.91	115	3.4	1.27	0.44	14	21.9	2.48	9.8	2.17	1.07	2.39	0.41	2.48	0.48	1.39	0.21	1.35	0.224	11.6
Poorly Amygdaloidal basalt	5,689.90	36	228	220	29	80	70	120	14	0.8	<5	65	443	741	35.3	3.52	129	3.4	1.81	0.53	16.2	32.8	4.1	17	3.72	1.27	4.13	0.66	4.04	0.78	2.37	0.352	2.32	0.363	21.6
Poorly Amygdaloidal basalt	5,690.20	29	215	220	30	90	70	60	15	1	<5	59	471	551	35	3.43	119	3.3	1.74	0.54	14.7	30.3	3.78	15.5	3.65	1.32	4	0.61	3.81	0.73	2.1	0.299	2.13	0.327	20.5
Amygdaloidal basalt	5,189.00	28	202	220	30	70	60	40	14	1	80	54	518	576	31.6	2.61	109	2.6	2.3	6.22	19.3	38.1	4.63	18.3	3.95	1.33	3.65	0.59	3.52	0.69	1.86	0.263	1.69	0.274	18.9
Amygdaloidal basalt	5,349.20	25	183	270	26	120	60	220	12	0.7	52	33	432	1,045	32.9	3.35	100	2.8	1.3	1.57	14.5	27.4	3.11	13.3	2.95	1.06	3.07	0.49	2.97	0.6	1.68	0.232	1.57	0.248	16
Amygdaloidal basalt	5,357.80	29	202	380	28	150	70	30	12	0.7	<5	37	462	355	37	3.81	109	3	1.47	0.83	13.4	26.7	3.33	13.6	3.12	1.05	3.17	0.55	3.26	0.65	1.85	0.276	1.83	0.283	17.6
Amygdaloidal basalt	5,367.40	27	187	190	22	70	60	30	13	0.8	14	38	502	671	35.1	3.6	106	2.8	1.41	2.62	12.8	25.3	3.1	12.3	2.86	1.03	3.12	0.51	3.23	0.65	2.06	0.299	1.85	0.288	17.2

(Continued on the following page)

10.3389/feart.2024.1497913

TABLE 2 (*Continued*)Whole rock trace element compositions of samples of borehole Well Y in Santos Basin.

Petrology	Depth	Sc	V	Cr	Co.	Ni	Cu	Zn	Ga	Ge	As	Rb	Sr	Ba	Nb	Ta	Zr	Hf	Th	U	La	Ce	Pr	Nd	Sm	Eu	Gd	Tb	Dy	Ho	Er	Tm	Yb	Lu	Y
Amygdaloidal basalt	5,372.90	26	184	240	24	100	60	60	11	0.5	14	44	433	760	32.8	3.49	100	2.8	1.42	0.99	13.1	25.4	3.04	12.9	3.11	1.01	3.22	0.51	3.01	0.62	1.82	0.26	1.7	0.251	16.2
Amygdaloidal basalt	5,432.00	29	224	130	25	70	70	60	15	0.9	32	44	251	787	33	3.73	102	3.3	1.74	5.13	14.9	29.4	3.67	14.2	3.28	1.17	3.18	0.56	3.35	0.66	1.89	0.269	1.68	0.264	17.1
Amygdaloidal basalt	5,447.20	30	230	100	24	70	70	40	15	0.9	23	32	716	627	40.3	4.15	132	3.8	1.92	5.81	16.9	34.4	4.32	18.1	4.12	1.38	4.28	0.69	4.15	0.83	2.41	0.344	2.24	0.376	22.8
Amygdaloidal basalt	5,570.10	25	154	230	28	100	80	<30	13	0.8	10	61	358	784	26.5	2.27	131	2.8	1.4	0.56	11.6	23.3	2.89	11.9	2.69	0.962	2.87	0.53	3.15	0.58	1.67	0.239	1.54	0.233	14.9
Amygdaloidal basalt	5,577.40	31	205	280	30	110	80	60	15	1.3	<5	21	758	418	26.5	2.37	100	2.6	1.34	0.35	16.5	28.6	3.18	12.6	2.92	1.15	3.34	0.54	3.23	0.65	1.88	0.282	1.75	0.275	18
Amygdaloidal basalt	5,620.10	29	216	330	39	140	80	<30	12	<0.5	17	52	222	393	29.7	2.93	94	2.6	1.77	2.62	12.3	25.9	3.24	14.4	3.2	1.18	3.23	0.52	3.19	0.66	1.81	0.275	1.76	0.279	17.6
Diabase	5,279.60	25	159	190	26	80	80	40	11	0.9	<5	4	465	121	10.6	0.97	50	1.4	0.58	0.31	6.23	13.5	1.86	8.12	2.24	0.838	2.67	0.45	2.69	0.55	1.62	0.221	1.43	0.251	14.9
Diabase	5,283.90	25	177	170	34	100	100	50	12	0.9	<5	6	317	157	13.8	1.25	66	1.6	0.75	0.19	7.78	16.6	2.15	9.81	2.59	0.956	2.85	0.47	3.03	0.64	1.87	0.261	1.67	0.259	17
Diabase	5,306.00	29	201	200	24	80	110	120	13	0.9	<5	14	322	417	13.8	1.22	66	1.6	0.82	0.18	8.83	18.1	2.28	10.4	2.78	1.03	3.15	0.53	3.29	0.69	1.88	0.289	1.97	0.3	17.5
Diabase	5,542.60	30	197	230	26	90	70	40	12	0.8	14	39	507	420	22.1	2.1	84	2.1	1.22	1.63	11.4	22.7	2.77	10.9	2.68	0.929	2.9	0.45	2.87	0.59	1.67	0.242	1.59	0.245	15.9
Diabase	5,572.70	29	192	260	32	120	80	50	12	0.8	11	26	531	510	23.9	2.25	83	2.2	1.31	1.68	11.8	23.3	2.8	11.6	2.85	0.996	2.91	0.5	3.01	0.6	1.76	0.257	1.7	0.27	16.9
Diabase	5,587.70	29	196	400	39	200	70	50	13	1	<5	15	266	247	26.9	2.49	98	2.4	1.46	0.35	12.1	24.2	3.09	12	3.2	1.02	3.17	0.54	3.25	0.64	1.86	0.28	1.83	0.293	17.5
Diabase	5,598.90	22	167	160	19	80	60	90	10	0.9	7	37	358	316	24.8	2.37	93	2.4	1.04	0.61	10.9	21.1	2.57	10.6	2.68	0.894	2.87	0.48	2.94	0.59	1.68	0.25	1.63	0.27	16.5
Diabase	5,604.10	29	222	220	32	110	80	70	14	0.8	7	48	479	559	36.6	3.64	133	3.3	1.55	1.07	15.2	30.5	3.67	15.3	3.67	1.28	3.92	0.64	3.83	0.74	2.13	0.314	2	0.319	20.7
Diabase	5,635.90	24	194	340	34	150	70	<30	11	0.9	16	47	243	1,053	25.9	2.62	100	2.7	1.34	0.96	12.5	25.8	3.24	13.3	3.24	1.18	3.23	0.55	3.28	0.63	1.74	0.256	1.72	0.27	17.3
Diabase	5,656.20	29	212	210	29	100	70	60	14	0.9	<5	75	392	3,730	32.3	3.32	121	3.1	1.37	0.34	14.3	27.5	3.1	12.6	3.18	1.03	3.39	0.57	3.37	0.65	1.95	0.294	1.92	0.321	18.6
Diabase	5,657.10	32	231	250	34	100	80	70	15	1.1	<5	54	294	2039	33.3	3.58	120	3.5	1.4	0.34	12.6	26.3	3.35	14.6	3.38	1.24	3.56	0.61	3.62	0.72	2.06	0.312	2.05	0.325	18.9
Diabase	5,658.20	23	161	160	19	80	50	<30	10	0.8	29	55	382	423	23.2	2.63	90	2.4	0.99	1.06	9.27	19.2	2.48	10.6	2.6	0.856	2.82	0.45	2.78	0.55	1.54	0.223	1.51	0.241	14.1
Diabase	5,666.20	18	167	150	32	120	70	30	12	0.6	12	78	203	765	34.5	3.16	124	3	1.53	0.95	10.8	22	2.82	11	2.67	1.05	3.02	0.51	2.99	0.61	1.81	0.263	1.76	0.277	16.7

(Continued on the following page)

10.3389/feart.2024.1497913

10.3389/feart.2024.1497913

TABLE 2 (*Continued*) Whole rock trace element compositions of samples of borehole Well Y in Santos Basin.

Petrology	Depth	Sc	V	Cr	Co.	Ni	Cu	Zn	Ga	Ge	As	Rb	Sr	Ba	Nb	Ta	Zr	Hf	Th	U	La	Ce	Pr	Nd	Sm	Eu	Gd	Tb	Dy	Ho	Er	Tm	Yb	Lu	Y
Diabase	5,671.30	29	239	230	29	90	80	120	14	0.7	16	66	183	584	35.5	3.53	119	3.4	1.8	3.69	14.8	31.1	3.95	16.7	3.9	1.13	3.94	0.69	4.07	0.81	2.4	0.352	2.37	0.372	22.6
Diabase	5,675.10	25	237	170	34	90	100	70	15	0.7	8	71	297	1,036	44.8	4.1	156	4.1	2.15	0.81	18.4	37.2	4.6	18.6	4.14	1.19	4.14	0.71	4.24	0.79	2.25	0.334	2.15	0.331	21.1
Diabase	5,704.00	37	266	210	23	60	80	40	19	1.6	<5	32	370	402	42.6	3.96	154	3.8	2.15	0.55	18.9	36.8	4.55	18.1	4.09	1.48	4.36	0.71	4.32	0.8	2.39	0.362	2.46	0.362	23.3
Diabase	5,708.80	33	229	250	31	100	70	70	16	1	<5	33	448	369	36.1	3.38	130	3.5	1.76	0.46	15	30.4	3.73	15.4	3.68	1.23	3.96	0.62	3.78	0.76	2.16	0.324	2.15	0.311	21
Diabase	5,716.40	31	233	200	31	90	80	70	14	0.6	11	31	369	315	39.7	3.79	142	3.7	2.03	1.08	16.5	33.5	4.21	16.3	3.85	1.14	4.01	0.65	3.81	0.73	2.08	0.297	2	0.321	20
Diabase	5,721.40	31	215	260	31	110	60	70	13	0.7	<5	44	243	270	30.2	3.04	117	3.2	1.72	0.38	13.9	28.6	3.53	14.9	3.36	1.2	3.57	0.6	3.61	0.71	2.05	0.304	2	0.297	18.4
Diabase	5,724.80	29	217	250	35	130	70	60	14	1.1	<5	50	456	768	37.7	3.79	139	3.7	2.03	0.59	17.1	35.1	4.32	18	3.98	1.38	4.25	0.7	4.1	0.81	2.38	0.338	2.07	0.324	21.7
Diabase	5,735.00	26	185	460	36	240	60	50	12	1	<5	38	271	354	25.9	2.57	92	2.4	1.33	0.31	11.9	23.9	2.89	11.9	2.93	1.05	3	0.49	3.05	0.59	1.67	0.246	1.6	0.255	15.3

with AR acetone for 30 min, followed by two more washes with distilled water for 45 min. The final cleaning step involved a 15-minute wash with AR ethanol in an ultrasonic bath. Once cleaned, the samples were air-dried, and grains were handpicked under a binocular microscope.

The selected samples were loaded onto a 21-pit aluminum disk along with the neutron fluence monitor Fish Canyon Sanidine, which has a known age of 28.201 ± 0.046 Ma as documented by Kuiper et al. (2008). The arrangement followed the geometry outlined in Vasconcelos et al. (2002). The irradiation disks were sealed with aluminum covers, wrapped in aluminum foil, and vacuum-sealed into a quartz vial. This vial was irradiated for 14 h on 18 June 2013, in the Cadmium-lined B-1 CLICIT facility at Oregon State University, which houses a TRIGA-type reactor. Age determinations were made using the decay constants reported by Steiger and Jäger (1977).

Post-irradiation, the samples were analyzed using laser ^{40}Ar-^{39}Ar heating, following the procedures detailed in Vasconcelos et al. (2002). Before analysis, the rock grains and fluence monitors were baked under vacuum at approximately 200°C for around 12 h to ensure cleanliness. Incremental heating of each sample was performed using a continuous-wave Ar-ion laser with a 2 mm wide defocused beam. The released gas fraction was purified through a cryocooled cold-trap at −125°C and two C-50 SAES Zr-V-Fe getters before being analyzed for Ar isotopes in a MAP215-50 mass spectrometer, which was equipped with a third getter.

System blanks and air pipettes were measured before and after each sample to ensure accuracy. The automation and analytical procedures were based on the works of Deino and Potts (1990), and Vasconcelos et al. (2002). The data were corrected for mass discrimination, nucleogenic interferences, and atmospheric contamination, following the methodologies of Vasconcelos et al. (2002) and using the "MassSpec Version 8.133" software developed by Alan Deino of the Berkeley Geochronology Centre.

For the calculation of mass spectrometer discrimination, a $^{40}Ar/^{36}Ar$ value of 298.56 ± 0.31 for atmospheric argon was applied, as Renne et al. (2009). The J-factors for each Al-disk were determined through laser total fusion analyses of 15 individual aliquots of the neutron fluence monitor, with each aliquot containing one to three crystals of Fish Canyon sanidine. The sensitivity of the mass spectrometer was calculated based on the analysis of an air pipette, yielding a Faraday sensitivity of 3.84 x 10^{-9} moles/nA. Additionally, the sensitivity of the Balzers 217 Electron Multiplier, with a gain of approximately 145,000, was measured to be around 4.5 x 10^{-14} moles/nA.

4 Results

4.1 Major elements of whole rocks

In our study, the samples are from underwater drilling cores, which means displaying high LOI in natural conditions is inevitable. We are aware of such a situation and have taken corresponding measures in data processing. Specifically, before using these samples for further analysis, adjustments were made as follows: (1) the LOI of

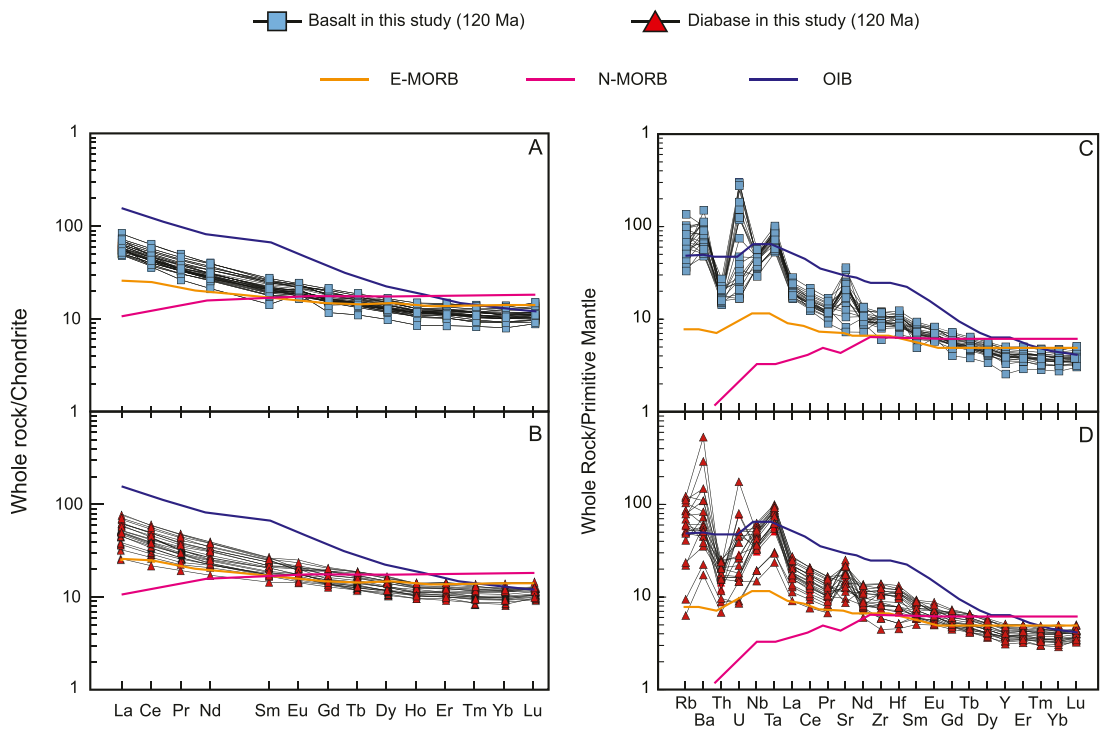

FIGURE 5
Rare earth elements **(A,B)** and trace element spidergram **(C,D)** for basalts and diabases of borehole Well Y in Santos Basin. The compositions of typical OIB, E-MORB, and N-MORB are from Sun and McDonough (1989).

all samples was subtracted from 100, (2) then dividing the result by the original total major elements value to get the correction factor, and (3) applying this factor to the original element concentrations to have the corrected data.

Original whole-rock major element data of samples in this study are shown in Table 1. The data indicate that the samples are mafic rocks, the SiO_2 contents range from 39.66% to 48.94% for basalts and 34.22%–47.93% for diabase. In the TAS (total alkalis vs. silica) discrimination diagram (Figure 4A), the basalts and most diabases plot in the alkaline basalt field, with exceptions that six samples of diabases plot in the subalkaline basalt. The MgO contents for basalts and diabase are 1.64%–8.27% and 2.11%–8.95%, respectively. Both basalts and diabases have variable Mg# (36.14–70.60 for basalts and 43.67–68.77 for diabase) and Na_2O+K_2O contents (4.30%–10.15% vs. 2.70%–9.58%).

4.2 Trace elements of whole rocks

The trace elements data of samples in this study are shown in Table 2. In Zr/Ti vs. Nb/Y (Figure 4B), basalts are homogeneous and plotted into the alkaline basalt field, consistent with the result of the TAS figure. For the diabase, the majority plot into the alkaline basalt field with some samples falling between basalt and alkaline basalt. Both basalts and diabases exhibit enriched LREE (Light Rare Earth Elements) (Figures 5A, B) and depleted HREE (Heavy Rare Earth Elements) (Figures 5C, D) patterns. However, basalts are more homogeneous in REE (Rare Earth Elements) and trace elements, with higher $(La/Yb)_N$ (4.5–8.2) rations than diabases (3.1–6.1). The large-ion lithophile elements (LILE) display an enriched pattern compared to high filed-strength elements (HFSE) in the primitive mantle-normalized multielement diagram. They all display enriched Ba, U, Ta, and Sr, but depleted Th.

4.3 Ar-Ar ages

The summaries of the $^{39}Ar/^{40}Ar$ age results are listed in Table 3. The Step-Heating age spectra are presented in Figure 6. Ar isotopic analysis results are shown in Supplementary Material. Five intervals of drilled igneous rocks yield Ar-Ar geochronological results. Incremental heating plateau ages are according to the definition of Fleck et al. (1977): "a sequence of two or more steps corresponding to a least 50% of the total ^{39}Ar released, the age values of which are within 2σ from the mean value calculated by weighting with inverse variance".

For intrusive rock, diabases have plateau ages ranging from 121.5 ± 0.2 Ma to 126.4 ± 1.0 Ma, consistent with isochron age, and older integrated age. At 5,279.6 m, the diabase whole rock fails to define a plateau, but the plagioclase grain yields reliable plateau age results. For extrusive rock, they have plateau ages from 110.8 ± 0.1 Ma to 116.6 ± 0.1 Ma. At 5,565.3 m, the basalt whole rock has no plateau or isochron result, but the plagioclase grain produced consistent results.

TABLE 3 Ar-Ar geochronological data of samples of borehole Well Y in Santos Basin.

Depth(m)	Sample	Emplacement	Microscopic description	Material	Plateau age (Ma)	1σ	Integrated age (Ma)	1σ	Isochron age (Ma)	1σ	Weighted mean age	1σ
5279.6	MBB-783	Intrusive	Diabase	WR	——	——	160.1	2.4	——	——	143.0	0.2
					——	——	151.5	1.9				
				Plagioclase	126.4	1.0	143.4	6.4	——	——	138.4	0.6
					125.9	1.8	142.8	9.4				
5283.9	MBB-784	Intrusive	Diabase	WR	125.8	0.7	152.1	1.0	125.7	1.3	129.4	0.1
					125.1	0.9	144.3	1.2				
5537.1	MBB-810	Extrusive subaqueous	Redeposited hyaloclastite	WR	116.6	0.1	111.6	0.7	117.9	1.0	99.8	0.1
					——	——	113.1	0.7				
5565.3	MBB-816	Extrusive subaqueous	Massive basalt	WR	——	——	93.0	0.6	——	——	83.3	0.1
					——	——	95.8	0.7				
				Plagioclase	111.2	0.1	109.9	0.4	——	——	108.1	0.1
					110.8	0.1	109.0	0.6				
5730.1	MBB-847	Intrusive	Diabase	WR	122.8	0.1	123.7	0.6	121.6	0.2	124.3	0.1
					123.2	0.2	124.2	0.9				
				Plagioclase	122.2	0.3	123.0	1.4	119.6	0.5	122.1	0.2
					121.5	0.2	122.2	1.2				

10.3389/feart.2024.1497913

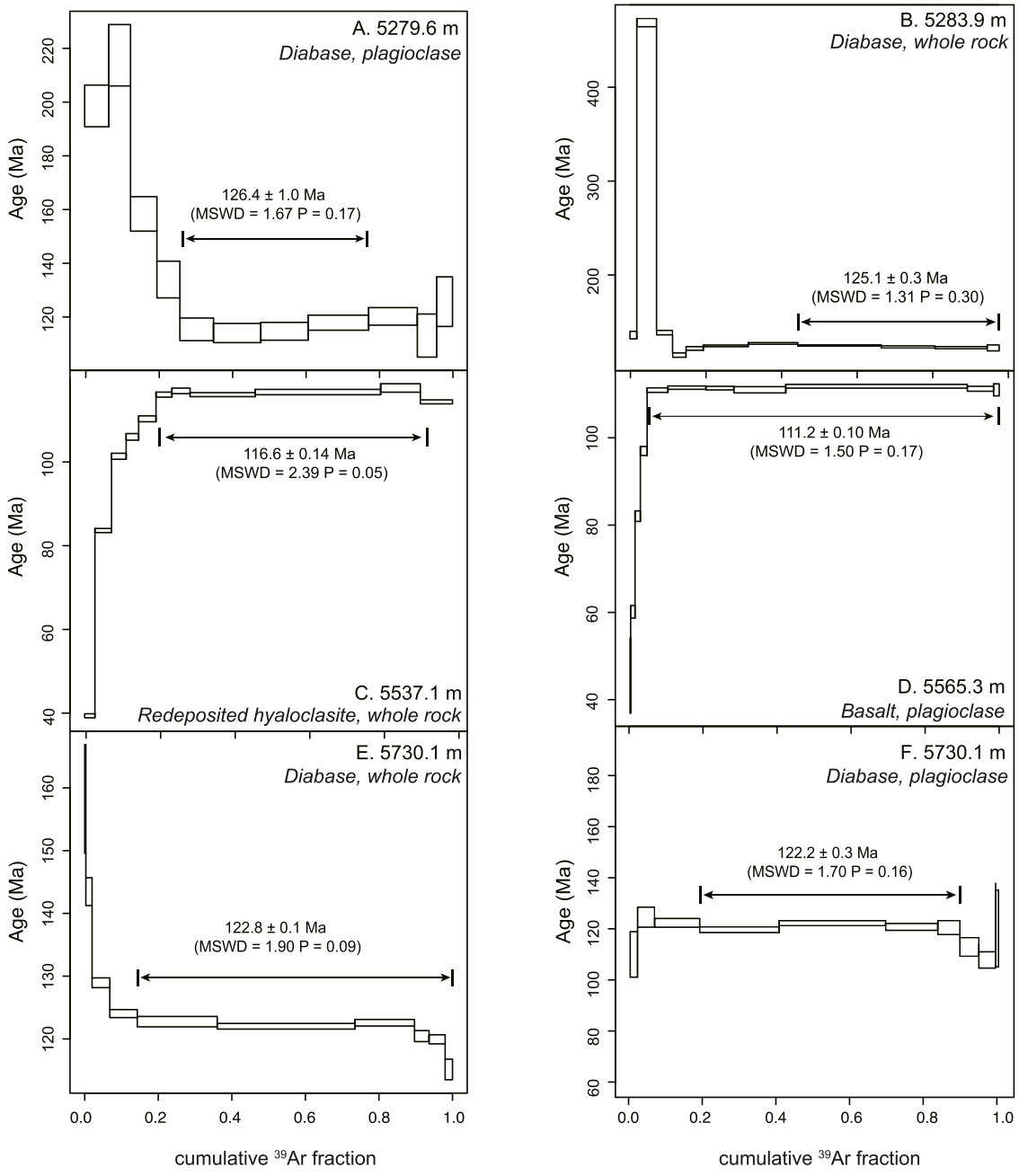

FIGURE 6
$^{40}Ar/^{39}Ar$ step-heating spectra in whole rock and plagioclase of basalts and diabases of borehole Well Y in Santos Basin. The plateau ages were the preferred Ar/Ar age for all samples.

4.4 Sr-Nd isotopic compositions

Ten samples including five basalts and five diabase were selected for isotope analyses, which are illustrated in Table 4. The Sr and Nd initial ratios were re-calculated to 120 Ma for both basalts and diabases. The $^{87}Sr/^{86}Sr_{(120\ Ma)}$ of basalts are higher than diabases, which are 0.708,556–0.709,684, and 0.704,609–0.708,292, respectively. The $\varepsilon Nd_{(120\ Ma)}$ of basalts and diabases are relatively homogeneous, +3.3 to +4.5 vs. +1.9 to +4.3.

5 Discussion

5.1 Age of basalts and diabases

Geochronological information of igneous rocks emplaced between sedimentary strata plays a significant role in revealing tectonic events and determining the formation sequence of strata. Igneous rocks, including both extrusive and intrusive facies, the extrusive basalt is younger than the sedimentary strata beneath it and older than the strata above; whereas the intrusive rocks

TABLE 4 Sr-Nd isotope ratios of samples of borehole Well Y in Santos Basin.

Depth	Lithofacies	Rb	Sr	$^{87}Rb/^{86}Sr$	$^{87}Sr/^{86}Sr(m)$	±2s	$^{87}Sr/^{86}Sr(i)$	Sm	Nd	$^{147}Sm/^{144}Nd$	$^{143}Nd/^{144}Nd(m)$	±2s	eNd(t)	$T_{DM}(Ga)$
5,553.5	Massive basalt	27	354	0.2207	0.709006	0.000014	0.708661	3.1	12.5	0.149937728399	0.512834	0.000001	4.5	0.54
5,432	Amygdaloidal basalt	44	251	0.5073	0.709378	0.000014	0.708556	3.28	14.2	0.13965082859	0.512822	0.000008	4.4	0.5
5,447.2	Amygdaloidal basalt	32	716	0.1293	0.709894	0.000014	0.709684	4.12	18.1	0.137618092072	0.512811	0.000005	4.2	0.51
5,620.1	Amygdaloidal basalt	52	222	0.6779	0.710654	0.000014	0.709556	3.2	14.4	0.134350712917	0.512768	0.000015	3.4	0.56
5,689.9	Poorly Amygdaloidal basalt	65	443	0.4246	0.709488	0.000014	0.708800	3.72	17	0.132295687812	0.51276	0.000019	3.3	0.56
5,708.8	Diabase	33	448	0.2131	0.708555	0.000014	0.708185	3.68	15.4	0.14446903607	0.512721	0.000002	2.4	0.72
5,724.8	Diabase	50	456	0.3173	0.708842	0.000014	0.708292	3.98	18	0.133677698834	0.512728	0.000003	2.7	0.62
5,283.9	Diabase	6	317	0.0547	0.705024	0.000014	0.704926	2.59	9.81	0.159616174621	0.512706	0.000011	1.9	0.93
5,587.7	Diabase	15	266	0.1631	0.704901	0.000014	0.704609	3.2	12	0.161223135837	0.512828	0.000006	4.3	0.66
5,657.1	Diabase	54	294	0.5313	0.706414	0.000014	0.705462	3.38	14.6	0.139964491047	0.512783	0.000006	3.7	0.57

The initial values have been calculated back to 120 Ma.

10.3389/feart.2024.1497913

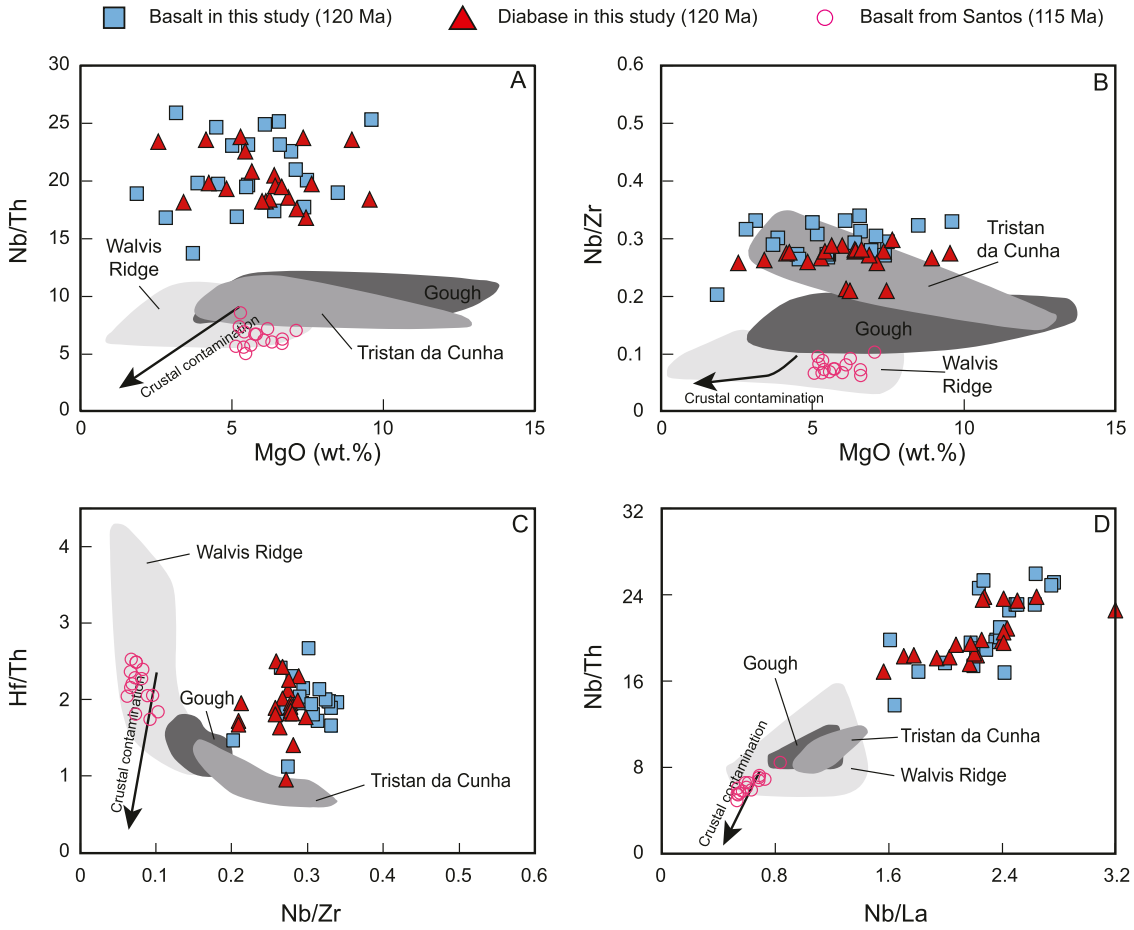

FIGURE 7
Major and trace element ratios relationship of basalts and diabases from borehole Well Y in Santos Basin. Data for 115 Ma basalts from Santos basin are from Louback et al. (2023). The crustal contamination line is from Marques et al. (2018). Lava flow are from the Walvis Ridges and the ocean islands of Tristan da Cunha and Gough are from Hoernle et al. (2015), Salters and Sachi-Kocher, (2010), Willbold and Stracke, (2010), Salters et al. (2011), Willbold & Stracke, (2010), and Weaver et al. (1987).

such as diabase are younger than existing strata, whether the strata are sedimentary or igneous. Therefore, the ages of basalts or diabases in the Santos basin serve as key indicators for understanding tectonic and depositional events. The intrusive diabases in this study are well-dated by the plagioclase Ar-Ar method. The results are reliable because the tested plagioclases in diabases are fresh. All the plateau ages range from 126 Ma to 121 Ma, suggesting that these diabases probably intruded during the same magmatic event.

In contrast, the ages of extrusive basalts in this study are unreliable. Basalt samples selected for whole rock and plagioclase Ar-Ar dating are strongly altered in the massive basalt and hyaloclastite. These basalts contain high concentrations of amygdaloids, which are filled with secondary minerals (e.g., carbonate, zeolites, and sulfides). Additionally, the plagioclase phenocrysts in massive basalt are intensely altered to sericite, and/or albite. Ar-Ar analysis reveals that these basalts have the ages of 116 Ma-110 Ma, dating approximately 10 Ma younger than the wrapped diabases from the same well. However, it is impossible that the older diabase intruded into the younger basalts 10 Ma later. Therefore, the basalts from the well in this study are not erupted around 116–110 Ma.

The only possible explanation for the relationship between extrusive basalts and intrusive diabases is that basalts are older than diabase or they occurred in the same magmatism. This hypothesis is supported by three key pieces of evidence: (1) all basalts are alkaline, whereas diabases range from alkaline to subalkaline. With basalts and diabases deriving from the same mantle source, and based on the rule that magma generally evolves from alkaline to subalkaline; (2) the partial melting degree of basalts is slightly lower than that of diabases. The lower-degree partial melted rocks are supposed to be older than those with a higher partial meting degree; (3) the cutting-through relationship between basalt and diabase also corroborates that the basalt should not be younger than diabase. Hence, the ages of basalts are supposed to be around 126–121 Ma, although further dating work is needed to verify. This stage of basalts erupted and then were covered by the limestone of ITP strata. Following that, the diabase then intruded into the basalts and limestone.

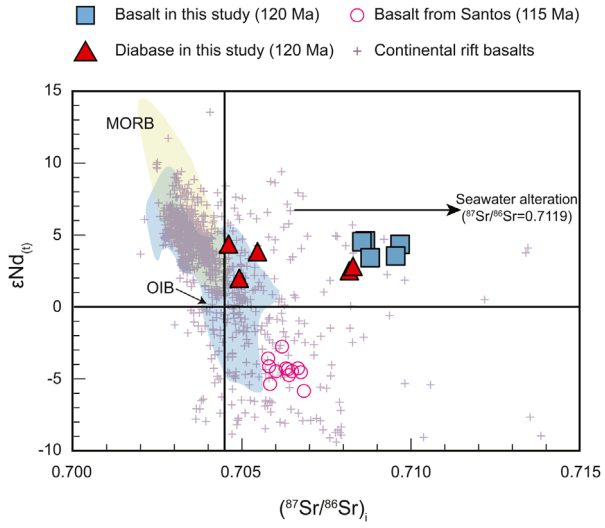

FIGURE 8
Whole-rock Sr-Nd isotopic compositions of basalts and diabases from borehole Well Y in Santos Basin. Data for 115 Ma basalts from Santos basin are from Louback et al. (2023). The data for MORB (mid-ocean ridge basalt), OIB, and CRB are from the Pet DB database (https://search.earthchem.org/). The Sr isotopic data for modern seawater is from Palmer and Edmond (1989).

5.2 Crustal contamination, seawater alteration, and fractional crystallization

Petrographic features and high loss on ignition values (greater than 6.2) indicate that the samples in this study have undergone varying degrees of alteration. The sequential stages of magma and post-magmatic processes play a crucial role in shaping the characteristics of igneous rocks and influence our ability to determine their origins. During magma processes, crustal contamination introduces variations in isotopic and trace element signatures, contingent upon the specific composition and volume of the rock that becomes assimilated. This stands in contrast to the post-magmatic alteration, characterized by the selective mobilization of the most soluble elements. After the initial magma formation and crystallization, subsequent magmatic alteration processes further modify the geochemical composition of the rock. The magmatic alteration processes may include crustal contamination and seawater alteration. Previous studies suggest that during crustal contamination and seawater alteration, some major and trace elements, such as Ti, Fe, Al, P, Mn, REEs, HFSEs (e.g., Zr, Nb, Ta, Ti, Th, and Y) and Nd isotopic ratios were not commonly transported or changed, while Mg, Ca, Na, K, LILEs (e.g., Sr, Ba and Rb), and Sr isotopic compositions were disturbed (Smith and Smith, 1976; Bédard, 1999). It is therefore important to further assess the influence of element mobility on the composition of samples in this study at the very beginning of the discussion.

Basalts with strong alkalinity have not been affected by significant crustal contamination, as magma with extensive alkalinity usually extrude rapidly, leaving little time for magma evolution or wall-rock assimilations. Although a small amount of diabases is subalkaline, all samples in this study show no decreasing trends of Nb/Zr and Nb/Th with decreasing MgO (Figures 7A, B). Similarly, the high Nb/Th and Nb/La of samples in this study display no similarity compared to crustal contaminated lavas (Figures 7C, D). All these characteristics suggest that whether basalts or diabases in this study are not strongly crustal contaminated.

However, samples in this study exhibit a wide range of radiogenic Sr compositions (0.704,609–0.709,684). Basalts have higher $^{87}Sr/^{86}Sr$ ratios (0.708,556–0.709,684), whereas diabases have a wider range of Sr isotopic ratios (0.704,609–0.708,292). Such a range of radiogenic Sr compositions are potentially resulted from crustal contamination and/or sea-water alteration (Dani et al., 2017). As discussed above, samples in this study are unlikely affected by crustal contamination, hence the widespread Sr compositions are the result of sea-water alteration (Figure 8). Samples in this study were collected from boreholes approximately 2000 m below sea surface, meaning inevitable interactions with seawater, and caused variations in their Sr isotopic compositions. The largest $^{87}Sr/^{86}Sr$ ratio, similar to that of modern seawater ($^{87}Sr/^{86}Sr$=0.7119; Palmer and Edmond, 1989), indicates that the hydrothermal alteration of seawater may account for the positive $^{87}Sr/^{86}Sr$ values of the Santos basalts and diabases. Therefore, the Sr isotopic compositions would not be discussed for their magma sources.

Both basalts and diabases have low SiO_2 (39.66%–48.94% for basalts and 34.22%–47.93% for diabases) contents, and no observable correlation is found between MgO and other oxides (Figure 9), suggesting negligible fractional crystallization of olivine and pyroxene (Zeng et al., 2010). The lack of a negative Eu anomaly suggests no significant removal of plagioclase. Therefore, the trace elements and Nd isotopic compositions of samples in this study are not influenced by AFC or other contamination processes, allowing for a more accurate discussion of their sources.

5.3 Mantle source

The basalts and diabases show similar chemical and Nd isotopic compositions where the Nd isotopic compositions are depleted and vary in a narrow range, pointing to potential similar source regions from the depleted mantle. Both basalts and diabases plotted far away from the plume magma (Figures 7A–D), thus the relationship between studied samples and 134 Ma Tristan da Cunha mantle plume is ruled out in the Santos basin. The REE fractionation in basalts can be used to estimate the depth and degree of mantle melting. In a Sm/Yb *versus* La/Sm diagram (Figure 10), modeling results suggest that the basalts and diabases in this study were sourced from the spinel + garnet (spinel/garnet>1) lherzolite facies. Compared with OIBs, the higher La/Sm ratio indicates a 1%–5% partial melting degree, similar to that of continental rift basalts. Additionally, it is worth mentioning that parts of the diabases show relatively higher partial melting degree, depicting a magma evolution trend. To gain a deeper understanding of the origin of basalts and diabases, basalts from a drill core adjacent to the sample location in this study were also plotted for comparison. Basalts from the well 4-BRSA-971B-SPS (Louback et al., 2023), erupted at around 115 Ma, are classified as subalkaline basalts, and are plotted into the continental rift basalt field. Compared with older basalts and diabases (126–121 Ma), they show signs of strong crustal contamination. With higher Sm/Yb and La/Yb ratios of adjacent samples, it's clear that these sub-alkaline basalts were sourced from

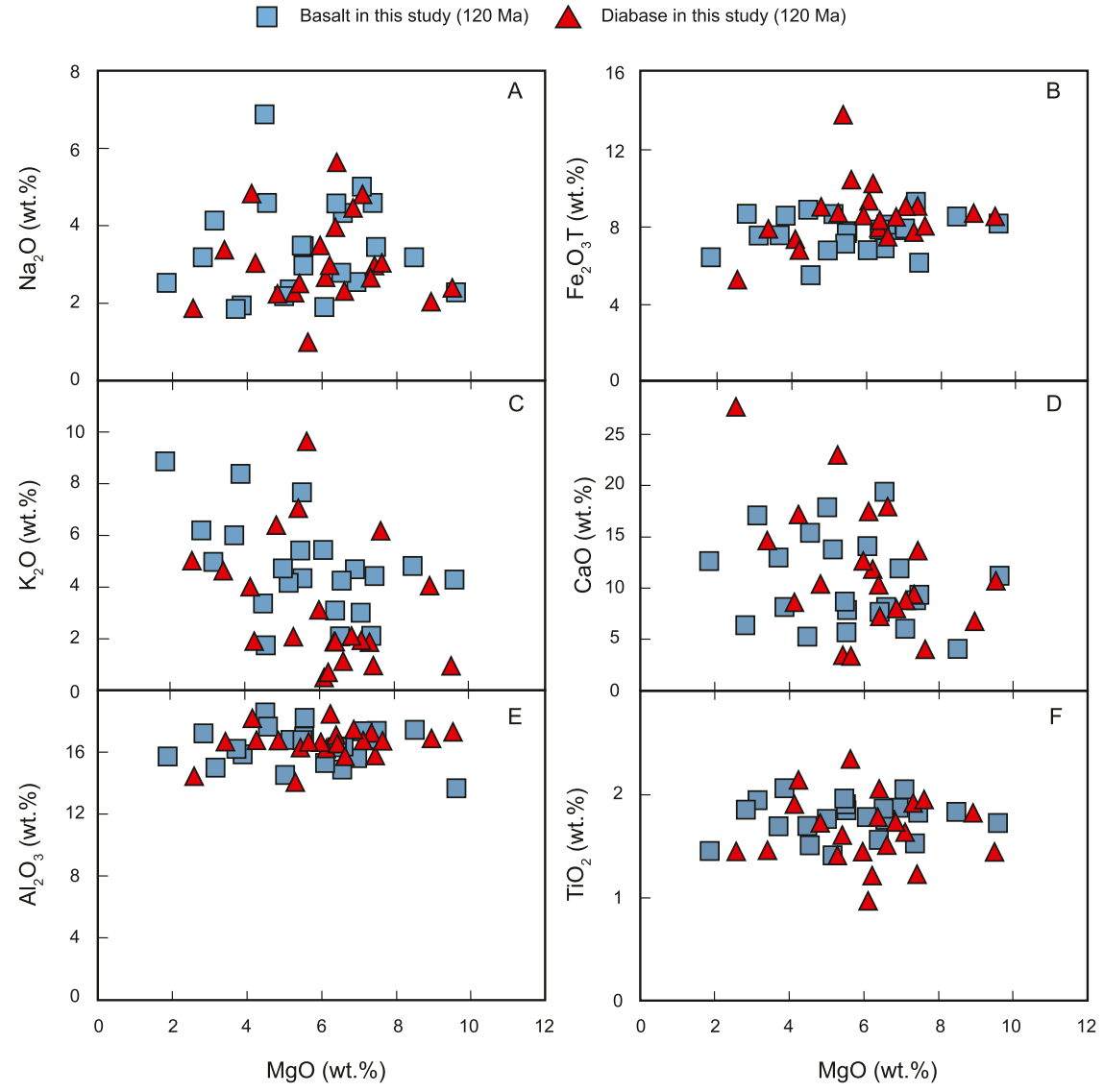

FIGURE 9
Variations in Na_2O **(A)**, Fe_2O_3 **(B)**, K_2O **(C)**, CaO **(D)**, Al_2O_3 **(E)**, TiO_2 **(F)** vs. MgO for basalts and diabases from borehole Well Y in Santos Basin.

spinel + garnet (spinel/garnet<1) lherzolite facies with a higher partial melting degree (5%–10%). The geochemical modeling results also suggest that the 115 Ma basalts have undergone partial melting within the garnet-spinel transition zone (Louback et al., 2023). Therefore, with time, the source region of magma deepens, and the degree of partial melting correspondingly increases. Reasoning from above, from the 126–121 Ma basalts to the slightly later diabases, then to the 115 Ma basalts, a magma transition from alkaline to sub-alkaline and the increased partial melting degree are revealed. And diabases represent the transitional process by showing both alkaline and sub-alkaline series. The elevated partial melting degree also suggests that the overlying lid above the magma was getting thinner from 126 Ma to 115 Ma.

The different chemical and isotopic compositions between 115 Ma and 126–121 Ma basalts suggest that they may derived from different mantle sources. Previous studies suggest that the 115 Ma basalts from the Santos Basin with enriched Sr-Nd-Hf-Pb isotopic compositions may be derived from an EMI mantle component in the subcontinental lithospheric mantle (SCLM). However, the Pb isotopic data published in Louback et al. (2023) are measured Pb ratios rather than initial ratios, which may affect its conclusions. Additionally, if the 115 Ma basalts are sourced from SCLM, thus the basalts and diabases emplaced in 126–121 Ma, whose source is shallower than that of 115 Ma basalts, would be derived from the shallow part of SCLM. However, the shallow part of SCLM, marked by enriched Sr-Nd isotopic compositions, is inconsistent with the depleted Nd isotopic compositions of 126–121 Ma basalts and diabases. Therefore, we suggest that basalts and diabases emplaced approximately 120 Ma may be derived from the asthenospheric mantle, and the source of 115 Ma basalts would be a deeper asthenospheric mantle with crustal contamination (Cohen and O'Nions, 1982; Louback et al., 2023) or the addition

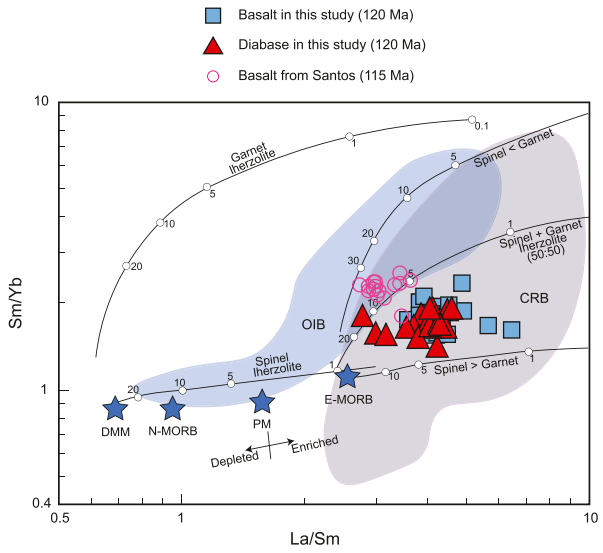

FIGURE 10
Variations in La/Sm vs. Sm/Yb for basalts and diabases from borehole Well Y in Santos Basin. Data for 115 Ma basalts from Santos Basin are from Louback et al. (2023). The field of global continental rift basalt (CRB) and Ocean Island basalts (OIB) are from the PetDB database (https://search.earthchem.org/). DMM, depleted mid-ocean ridge basalt mantle; PM, primitive mantle, N-MORB, normal mid-ocean ridge basalt, E-MORB, enriched mid-ocean ridge basalt.

of the SCLM (McKenzie and O'Nions, 1983). The decreasing trends of Nb/Zr and Nb/Th with decreasing MgO (Figure 7) along with the correlation of Hf/Th vs. Nb/Zr, and Nb/Th vs. Nb/La (Figure 7), further support that the 115 Ma basalts are strongly contaminated by the crust. The addition of enriched crustal material would produce enriched Sr-Nd-Hf-Pb isotopic compositions for 115 Ma basalts. Though the continental crust is rather thicker at 126 Ma, the alkaline basalts ascended rapidly, leaving little chance for crustal contamination. In contrast, the subalkaline basalts have a lower ascending speed, which is necessary to be affected by crustal materials.

5.4 Geodynamic

Santos originated as a rift basin during the break-up of Gondwana in the Lower Cretaceous and evolved into a passive margin basin during the opening of the South Atlantic Ocean (Chang et al., 1992; Cainelli and Mohriak, 1999). Magmatic processes in the Santos basin evolved from rift, post-rift, and drift sedimentary mega-sequences (Fodor and Vetter, 1984; Heilbron et al., 2000; Moreira et al., 2006).

The Tristan da Cunha plume in Parana-Etendeka Magmatic province is always thought to be the genesis of rift magmatism in the Santos Basin (e.g., Gibson et al., 1995; Milner and Le Roex, 1996), and melting of rift or post-rift magma is possible due to heat conduction of the underlain or remaining heat advected by Tristan da Cunha mantle plume. However, neither pre-rift magma nor 126–121 Ma or 115–110 Ma samples in this and previous study (e.g., Peate, 1997; Marques, et al., 1999; Ernesto et al., 2002; Rocha-Júnior et al., 2013; Louback et al., 2023) show plume's origin (Figure 7). The geochronological result also suggests that the duration of the Parana volcanism lasted merely 1.2 Ma (Thiede and Vasconcelos, 2010), indicating that Tristan da Cunha may not be the origin for the post-rift magmatic event. Although seismic tomographic data suggested that there was a long-living deep mantle thermal anomalies in the Santos Basin (Ernesto et al., 2002; Ernesto, 2005; Celli et al., 2020), the mantle plume primarily contributes heat rather than altering the composition.

The geochemical signatures of the basalts and diabases from the Santos Basin indicate partial melting of spinel + garnet lherzolite facies. High La/Sm ratios and low partial melting degrees (1%–5%) suggest continental rift magmatic processes. Older basalts likely originated from the asthenosphere, while younger ones show mixing signs between SCLM or crustal material and the deeper asthenosphere. Similar patterns are observed in the East African Rift and Basin and Range Province. These findings indicate significant lithospheric thinning and stretching during the post-rift phase, deepening of the basin into the asthenosphere and causing magmatic activities. A hypothetical model with cross-sectional diagrams, explains the tectonic and magmatic evolution of the basin (Figure 11). During 126–121 Ma, Tristan da Cunha mantle plume heats the overlying lithosphere, resulting in its softening. Continental extending due to the continental rift process produced alkaline basalts, which sourced from the asthenospheric mantle after 1%–5% partial melting, then erupted to the surface and overlapped the existing strata. Nearly simultaneously, or shortly after the basalt formed, alkaline and subalkaline diabase intruded into basalts. Due to the high ascending speed of alkaline magma, they are rarely affected by crustal material. During 115–110 Ma, the softened continental lithosphere was thinning along with the basin expanding due to the continuous continental extension, subcontinental lithospheric mantle may be delaminated into the asthenosphere. Subalkaline basalts derived from deeper asthenosphere mixed with these delaminated SCLM erupted to the surface. These subalkaline basalts have enriched Sr-Nd-Hf isotopic compositions and experienced 5%–10% partial melting. As a result of their reduced ascent rate, crustal contamination is inevitable. The Santos post-rift process was from 126 Ma to 110 Ma, with magma evolving from alkaline to subalkaline and the partial melting degree increased. The source of magma transformed from a shallower, depleted asthenospheric mantle to a deeper, enriched asthenospheric mantle mixed with subcontinental lithospheric mantle or contaminated by crustal material. These characteristics collectively suggest that the continental rift deepened to the asthenosphere along with stretching (Figure 11). Meanwhile, the continental lithosphere underneath Santos was getting thinner, which can be delaminated into the asthenosphere.

6 Conclusion

This study conducts an in-depth petrogenic and geochemical analysis of the basalts and diabases from the Santos Basin, dated approximately ~126–121 Ma. It sheds new light on the magmatic and tectonic evolution of passive continental margin basins. The rocks are derived from the partial melting of spinel

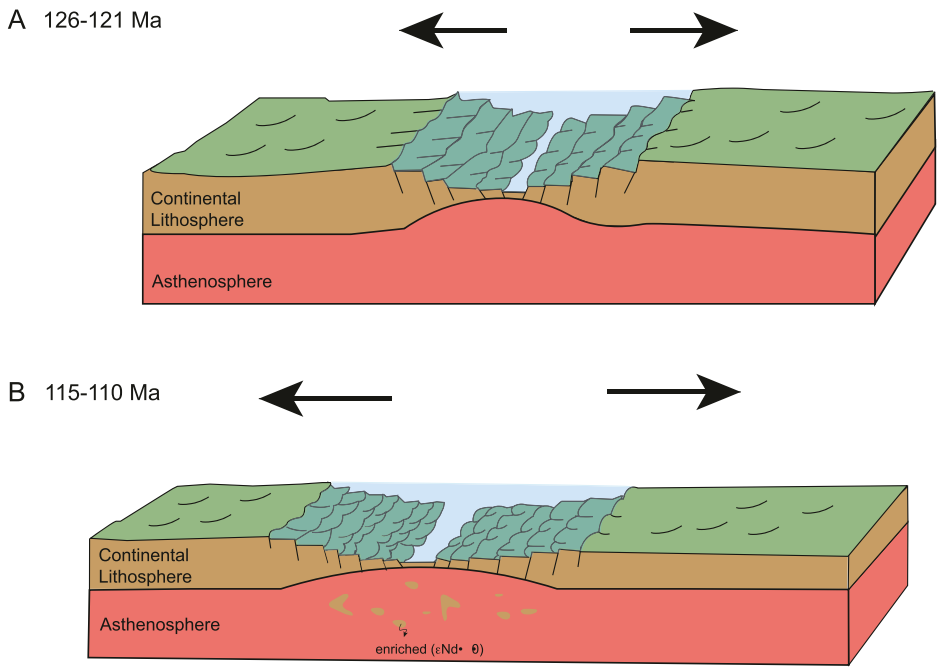

FIGURE 11
Geodynamic conceptual model for the post-rift tectonic evolution from 126–121 Ma **(A)** to 115–110 Ma **(B)** in Santos Basin.

and garnet lherzolite, with the early basalts originating from the asthenosphere, while later ones exhibit characteristics of a mix between the asthenosphere and the SCLM. The geological model suggests that basin deepening and lithospheric thinning were pivotal in triggering magmatic activity. These findings further expand horizons in understanding the magmatic histories of similar basins worldwide, emphasizing the role of asthenospheric-lithospheric interactions and the significance of basin dynamics in modulating magmatic events.

Data availability statement

The datasets presented in this study can be found in online repositories. The names of the repository/repositories and accession number(s) can be found in the article/supplementary material.

Author contributions

WH: Writing–review and editing. HW: Writing–review and editing. JS: Data curation, Writing–review and editing. WW: Investigation, Writing–review and editing. JuZ: Data curation, Writing–review and editing. GZ: Data curation, Writing–review and editing. TW: Data curation, Writing–review and editing. LY: Investigation, Writing–review and editing. KR: Data curation, Writing–review and editing. CW: Writing–review and editing. JiZ: Data curation, Writing–review and editing. YG: Conceptualization, Writing–review and editing. YZ: Conceptualization, Writing–review and editing. JS: Writing–original draft, Writing–review and editing.

Funding

The author(s) declare that no financial support was received for the research, authorship, and/or publication of this article.

Conflict of interest

Authors WH and WW were employed by China National Oil and Gas Exploration and Development Corporation. Authors HW, GZ, LY, CW, and YZ were employed by PetroChina Hangzhou Research Institute of Geology. Authors JuZ, TW, KR, JiZ and YG were employed by CNPC Brasil Petroleo e Gas Ltda.

The remaining authors declare that the research was conducted in the absence of any commercial or financial relationships that could be construed as a potential conflict of interest.

Publisher's note

References

Adriano, M. S., Figueiredo, J. P., Coelho, P. H. G. R., and Borghi, L. (2022). Tectonic and stratigraphic evolution of the Santos Basin rift phase: new insights from seismic interpretation on Tupi oil field area. *J. S. Am. Earth Sci.* 116, 103842. doi:10.1016/j.jsames.2022.103842

Almeida, F. F. M., Hasui, Y., de Brito Neves, B. B., and Fuck, R. (1981). Brazilian structural provinces: an introduction. *Earth-Science Rev.* 17 (1-2), 1–29. doi:10.1016/0012-8252(81)90003-9

Almeida, J., Dios, F., Mohriak, W. U., Valeriano, C. D. M., Heilbron, M., Eirado, L. G., et al. (2013). Pre-Rift tectonic scenario of the eo-cretaceous Gondwana break-up along SE Brazil–sw africa: insights from tholeiitic mafic dyke swarms. *Geol. Soc. Lond. Spec. Publ.* 369 (1), 11–40. doi:10.1144/SP369.24

Almeida, J., Heilbron, M., Guedes, E., Neubauer, F., Manfred, B., Klausen, M. B., et al. (2021). Pre-to-syn-rift tholeiitic magmatism in A transtensive hyperextended continental margin: onshore and offshore magmatism of the campos basin, SE Brazil. *J. S. Am. Earth Sci.* 108, 103218. doi:10.1016/j.jsames.2021.103218

Bédard, J. H. (1999). Petrogenesis of boninites from the betts cove ophiolite, newfoundland, Canada: identification of subducted source components. *J. Petrology* 40 (12), 1853–1889. doi:10.1093/petroj/40.12.1853

Brito Neves, B. B. D., and Fuck, R. A. (2014). The basement of the South American platform: half laurentian (N-NW)+ half gondwanan (E-SE) domains. *Precambrian Res.* 244, 75–86. doi:10.1016/j.precamres.2013.09.020

Bruhn, C. H. L., Pinto, A. C. C., Johann, P. R. S., et al. (2017). "Campos and Santos basins: 40 Years of reservoir characterization and management of shallow- to ultra-deep water, post- and pre-salt reservoirs - historical overview and future challenges," in Offshore Technology Conference, Brazil, October 2017 (OTC), D011S006R001. doi:10.4043/28159-MS

Cai, Y., Rioux, M., Kelemen, P. B., Goldstein, S. L., Bolge, L., and Kylander-Clark, A. R. (2015). Distinctly different parental magmas for calc-alkaline plutons and tholeiitic lavas in the central and eastern aleutian arc. *Earth Planet. Sci. Lett.* 431, 119–126. doi:10.1016/j.epsl.2015.07.058

Cainelli, C., and Mohriak, W. U. (1999). General evolution of the eastern Brazilian continental margin. *Lead. Edge* 18 (7), 800–805. doi:10.1190/1.1438387

Carlotto, M. A., Da Silva, R. C. B. D., Yamato, A. A., Trindade, W. L., Moreira, J. L. P., Fernandes, R. A. R., et al. (2017). Libra: a newborn giant in the Brazilian presalt province. 165, 176. doi:10.1306/13572006M1133685

Celli, N. L., Lebedev, S., Schaeffer, A. J., Ravenna, M., and Gaina, C. (2020). The upper mantle beneath the South Atlantic Ocean, south America and africa from waveform tomography with massive data sets. *Geophys. J. Int.* 221 (1), 178–204. doi:10.1093/gji/ggz574

Chang, H. K., Assine, M. L., Corrêa, F. S., et al. (2008). Petroleum systems and hydrocarbon accumulation models in the Santos Basin. *Braz. J. Geol.* 38 (2), 29–46.

Chang, H. K., Kowsmann, R. O., Figueiredo, A. M. F., and Bender, A. (1992). Tectonics and stratigraphy of the East Brazil rift system: an overview. *Tectonophysics* 213 (1-2), 97–138. doi:10.1016/0040-1951(92)90253-3

Cohen, R. S., and O'Nions, R. K. (1982). Identification of recycled continental material in the mantle from Sr, Nd and Pb isotope investigations. *Earth Planet. Sci. Lett.* 61 (1), 73–84. doi:10.1016/0012-821X(82)90040-1

Dani, A. P. D. O., Remus, M. V. D., Dani, N., and Lima, E. F. d. (2017). Magmatismo BasÁltico do andar alagoas (bacia de campos). *Geol. Usp. Série Científica* 17 (2), 269–287. doi:10.11606/issn.2316-9095.v17-373

Dantas, E. L., Van Schmus, W. R., Hackspacher, P. C., Fetter, A., de Brito Neves, B., Cordani, U., et al. (2004). The 3.4–3.5 Ga são josé do campestre massif, NE Brazil: remnants of the oldest crust in South America. *Precambrian Res.* 130 (1-4), 113–137. doi:10.1016/j.precamres.2003.11.002

Deino, A., and Potts, R. (1990). Single-crystal $^{40}Ar/^{39}Ar$ dating of the olorgesailie formation, southern Kenya rift. *J. Geophys. Res. Solid Earth* 95 (B6), 8453–8470. doi:10.1029/JB095iB06p08453

Ernesto, M. (2005). "Paleomagnetism of the post-paleozoic alkaline magmatism in the Brazilian platform: questioning the mantle plume model," in *Mesozoic to cenozoic alkaline magmatism in the Brazilian platform* (São Paulo: Edusp/Fapesp), 689–705.

Ernesto, M., Marques, L. S., Piccirillo, E. M., Molina, E., Ussami, N., Comin-Chiaramonti, P., et al. (2002). ParanÁ magmatic province–tristan da Cunha plume system: fixed versus mobile plume, petrogenetic considerations and alternative heat sources. *J. Volcanol. Geotherm. Res.* 118 (1-2), 15–36. doi:10.1016/S0377-0273(02)00248-2

Evain, M., Afilhado, A., Rigoti, C., Loureiro, A., Alves, D., Klingelhoefer, F., et al. (2015). Deep structure of the Santos Basin-são Paulo Plateau system, SE Brazil. *J. Geophys. Res. Solid Earth* 120 (8), 5401–5431. doi:10.1002/2014JB011561

Filho, A. T., Mizusaki, A. M. P., et al. (2000). Rifting and magmatism associated with the South America and africa break up. *Braz. J. Geol.* 30 (1), 017–019.

Fleck, R. J., Sutter, J. F., and Elliot, D. H. (1977). Interpretation of discordant $^{40}Ar/^{39}Ar$ age-spectra of mesozoic tholeiites from Antarctica. *Geochimica Cosmochimica Acta* 41 (1), 15–32. doi:10.1016/0016-7037(77)90184-3

Fodor, R. V., and Vetter, S. K. (1984). Rift-zone magmatism: petrology of basaltic rocks transitional from CFB to MORB, southeastern Brazil margin. *Contributions Mineralogy Petrology* 88, 307–321. doi:10.1007/BF00376755

Ganade de Araujo, C. E., Weinberg, R. F., and Cordani, U. G. (2014). Extruding the borborema province (ne-Brazil): a two-stage neoproterozoic collision process. *Terra nova.* 26 (2), 157–168. doi:10.1111/ter.12084

Gibson, S. A., Thompson, R. N., Leonardos, O. H., Dickin, A. P., and Mitchell, J. G. (1995). The late cretaceous impact of the trindade mantle plume: evidence from large-volume, mafic, potassic magmatism in SE Brazil. *J. Petrology* 36 (1), 189–229. doi:10.1093/petrology/36.1.189

Gordon, A. C., Mohriak, W. U., Santos, A. C., Caitano, C. R., and Stanton, N. (2023). Magmatic cycles in santos basin (S.E. Brazil): geochemical characterization and magmatic sources. *J. S. Am. Earth Sci.* 126. doi:10.1016/j.jsames.2023.104323

Gudmundsson, A., and Løtveit, I. F. (2014). Sills as fractured hydrocarbon reservoirs: examples and models. *Geol. Soc. Lond. Spec. Publ.* 374 (1), 251–271. doi:10.1144/SP374.5

Heilbron, M., Mohriak, W. U., Valeriano, C. M., Milani, E. J., Almeida, J., and Tupinambá, M. (2000). From collision to extension: the roots of the southeastern continental margin of Brazil. *Atl. rifts Cont. margins* 1, 1–32. doi:10.1029/GM115p0001

Heilbron, M., Valeriano, C. M., Tassinari, C. C. G., Almeida, J., Tupinambá, M., Siga, O., jr, et al. (2008). Correlation of neoproterozoic terranes between the Ribeira Belt, SE Brazil and its african counterpart: comparative tectonic evolution and open questions. *Geol. Soc. Lond. Spec. Publ.* 294 (1), 211–237. doi:10.1144/SP294.12

Hoernle, K., Rohde, J., Hauff, F., Garbe-Schönberg, D., Homrighausen, S., Werner, R., et al. (2015). How and when plume zonation appeared during the 132 Myr evolution of the tristan hotspot. *Nat. Commun.* 6 (1), 7799–7810. doi:10.1038/ncomms8799

Kuiper, K., Deino, A., Hilgen, F., Krijgsman, W., Renne, P. R., and Wijbrans, J. R. (2008). Synchronizing rock clocks of earth history. *Science* 320 (5875), 500–504. doi:10.1126/science.1154339

Le Bas, M., Le Maitre, R., Streckeisen, A., and Zanettin, B. (1986). A chemical classification of volcanic rocks based on the total alkali–silica diagram. *J. Petrology* 27 (3), 745–750. doi:10.1093/petrology/27.3.745

Le Maitre, R., Streckeisen, A., Zanettin, B., et al. (2002). *Igneous rocks. A classification and glossary of terms: recommendations of the international union of geological Sciences subcommission on the Systematics of igneous rocks*. Cambridge: Cambridge University Press.

Li, C., Wang, X., Guo, J., Chu, Z. Y., and Feng, L. J. (2016). Rapid separation scheme of Sr, Nd, Pb, and Hf from A single rock digest using A tandem chromatography column prior to isotope ratio measurements by mass spectrometry. *J. Anal. Atomic Spectrom.* 31 (5), 1150–1159. doi:10.1039/C5JA00477B

Louback, V. S., De Castro Valente, S., De Almeida, C. N., Ross, J., and Borghi, L. (2023). Aptian flood basalts in bacalhau oil and gas field: petrogenesis and geodynamics of Post-Rift tholeiites in the pre-salt sequence of Santos Basin, Brazil. *Contributions Mineralogy Petrology* 178 (3), 15. doi:10.1007/s00410-023-01995-0

Marins, G. M., Parizek-Silva, Y., Millett, J. M., Jerram, D. A., Rossetti, L. M., e Sousa, A. d. J., et al. (2022). Characterization of volcanic reservoirs; insights from the badejo and linguado oil field, campos basin, Brazil. *Mar. Petroleum Geol.* 146, 105950. doi:10.1016/j.marpetgeo.2022.105950

Marques, L. S., De Min, A., Rocha-Júnior, E. R. V., Babinski, M., Bellieni, G., and Figueiredo, A. (2018). Elemental and Sr-Nd-Pb isotope geochemistry of the FlorianÓpolis dyke swarm (ParanÁ magmatic province): crustal contamination and mantle source constraints. *J. Volcanol. Geotherm. Res.* 355, 149–164. doi:10.1016/j.jvolgeores.2017.07.005

Marques, L. S., Ulbrich, M. N. C., Ruberti, E., and Tassinari, C. G. (1999). Petrology, geochemistry and Sr–Nd isotopes of the trindade and martin vaz volcanic rocks (southern Atlantic Ocean). *J. Volcanol. Geotherm. Res.* 93 (3-4), 191–216. doi:10.1016/S0377-0273(99)00111-0

McKenzie, D., and O'Nions, R. K. (1983). Mantle reservoirs and Ocean Island basalts. *Nature* 301 (5897), 229–231. doi:10.1038/301229a0

Milner, S. C., and Le Roex, A. P. (1996). Isotope characteristics of the okenyenya igneous complex, northwestern Namibia: constraints on the composition of the early tristan plume and the origin of the EM 1 mantle component. *Earth Planet. Sci. Lett.* 141 (1-4), 277–291. doi:10.1016/0012-821X(96)00074-X

Mio, E., Chang, H. K., and Corrêa, F. S. (2005). Integração de métodos geofísicos na modelagem crustal da Bacia de Santos. *Rev. Bras. Geof* 23 (3), 275–284. doi:10.1590/s0102-261x2005000300006

Mohriak, W. U., Macedo, J. M., Castellani, R. T., et al. (1995). *Salt tectonics and structural styles in the deep water province of the Cabo Frio region*. Brazil: Rio De Janeiro. doi:10.1306/M65604C13

Mohriak, W. U., and Rosendahl, B. R. (2003). Transform zones in The South atlantic rifted continental margins. *Geol. Soc. Lond. Spec. Publ.* 210 (1), 211–228. doi:10.1144/GSL.SP.2003.210.01.13

Moreira, J. L. P., Esteves, C. A., Rodrigues, J. J. G., et al. (2006). Magmatism, sedimentation, and stratigraphy of the northern portion of the Santos Basin. *Bull. Geosciences Petrobras, Rio J.* 14, 161–170.

Moreira, J. L. P., Madeira, C. V., Gil, J. A., et al. (2007). Santos Basin. *Bull. Geosciences Petrobras* 15, 531–549.

Palmer, M. R., and Edmond, J. M. (1989). The strontium isotope budget of the modern ocean. *Earth Planet. Sci. Lett.* 92 (1), 11–26. doi:10.1016/0012-821X(89)90017-4

Peate, D. W. (1997). The paraná-etendeka province. *Geophys. Monograph-American Geophys. Union* 100, 217–245. doi:10.1029/GM100p0217

Ren, K., Zhao, J., Liu, Q., et al. (2020). Hydrocarbons in igneous rock of Brazil: a review. *Petrol Res.* 5 (3), 265–275. doi:10.1016/j.ptlrs.2020.06.001

Renne, P. R., Cassata, W. S., and Morgan, L. E. (2009). The isotopic composition of atmospheric argon and $^{40}Ar/^{39}Ar$ geochronology: time for A change? *Quat. Geochronol.* 4 (4), 288–298. doi:10.1016/j.quageo.2009.02.015

Rocha-Júnior, E. R. V., Marques, L. S., Babinski, M., Nardy, A. J., Figueiredo, A. M., and Machado, F. B. (2013). Sr–Nd–Pb isotopic constraints on the nature of the mantle sources involved in the genesis of the high-Ti tholeiites from northern ParanÁ continental flood basalts (Brazil). *J. S. Am. Earth Sci.* 46, 9–25. doi:10.1016/j.jsames.2013.04.004

Rollinson, H. R. (1993). A terrane interpretation of the archaean limpopo Belt. *Geol. Mag.* 130 (6), 755–765. doi:10.1017/S001675680002313X

Salters, V. J. M., Mallick, S., Hart, S. R., Langmuir, C. E., and Stracke, A. (2011). Domains of depleted mantle: new evidence from hafnium and neodymium isotopes. *Geochem. Geophys. Geosystems* 12 (8). doi:10.1029/2011GC003617

Salters, V. J. M., and Sachi-Kocher, A. (2010). An ancient metasomatic source for the Walvis ridge basalts. *Chem. Geol.* 273 (3-4), 151–167. doi:10.1016/j.chemgeo.2010.02.010

Senger, K., Millett, J., Planke, S., Ogata, K., Haug Eide, C., Festøy, M., et al. (2017). Effects of igneous intrusions on the petroleum system: a review. *First Break* 35 (6). doi:10.3997/1365-2397.2017011

Smith, R. E., and Smith, S. E. (1976). Comments on the use of Ti, Zr, Y, Sr, K, P and Nb in classification of basaltic magmas. *Earth Planet. Sci. Lett.* 32 (2), 114–120. doi:10.1016/0012-821X(76)90049-2

Stanton, N., Ponte-Neto, C., Bijani, R., Masini, E., Fontes, S., and Flexor, J. M. (2014). A geophysical view of the southeastern Brazilian margin at Santos Basin: insights into rifting evolution. *J. S. Am. Earth Sci.* 55, 141–154. doi:10.1016/j.jsames.2014.07.003

Steiger, R. H., and Jäger, E. (1977). Subcommission on geochronology: convention on the use of decay constants in geo- and cosmochronology. *Earth Planet. Sci. Lett.* 36 (3), 359–362. doi:10.1016/0012-821X(77)90060-7

Streckeisen, A. (1978). IUGS subcommission on the Systematics of igneous rocks. Classification and nomenclature of volcanic rocks, lamprophyres, carbonatites and melilite rocks. Recommendations and suggestions. Neues jahrbuch Fur mineralogie. Stuttgart. *Abhandlungen* 143, 1–14.

Sun, S. S., and McDonough, W. F. (1989). Chemical and isotopic Systematics of oceanic basalts: implications for mantle composition and processes. *Geol. Soc. Lond. Spec. Publ.* 42 (1), 313–345. doi:10.1144/GSL.SP.1989.042.01.19

Tanaka, T., Togashi, S., Kamioka, H., Amakawa, H., Kagami, H., Hamamoto, T., et al. (2000). JNdi-1: a neodymium isotopic reference in consistency with lajolla neodymium. *Chem. Geol.* 168 (3-4), 279–281. doi:10.1016/S0009-2541(00)00198-4

Thiede, D. S., and Vasconcelos, P. M. (2010). ParanÁ flood basalts: rapid extrusion hypothesis confirmed by new $^{40}Ar/^{39}Ar$ results. *Geology* 38 (8), 747–750. doi:10.1130/G30919.1

Vasconcelos, P. M., Onoe, A. T., Kawashita, K., Soares, A. J., and Teixeira, W. (2002). $^{40}Ar/^{39}Ar$ geochronology at the Institute of geosciences, USP: instrumentation, analytical procedures, and calibration. *Ann. Braz. Acad. Sci.* 74, 297–342. doi:10.1590/S0001-37652002000200008

Wang, Z. C., Yang, T. Y., Chen, J. H., et al. (2019). Discussion on the development models of deepwater pre-salt oil fields in Brazil and their reference significance for the development of deepwater oil and gas fields in the South China sea, China. *China Offshore Oil Gas* 31, 155–159.

Weaver, B. L., Wood, D. A., Tarney, J., and Joron, J. L. (1987). Geochemistry of Ocean Island basalts from the South atlantic: ascension, bouvet, st. Helena, Gough and tristan da Cunha. *Geol. Soc. Lond. Spec. Publ.* 30 (1), 253–267. doi:10.1144/gsl.sp.1987.030.01.11

Weis, D., and Frey, F. A. (1996). Role of the kerguelen plume in generating the eastern Indian ocean seafloor. *J. Geophys. Res. Solid Earth* 101 (B6), 13831–13849. doi:10.1029/96JB00410

Weis, D., Frey, F. A., Saunders, A., and Gibson, I. (1991). Ninetyeast Ridge (Indian ocean): a 5000 Km record of A dupal mantle plume. *Geology* 19 (2), 99–102. doi:10.1130/0091-7613(1991)019<0099:nrioak>2.3.co;2

Willbold, M., and Stracke, A. (2010). Formation of enriched mantle components by recycling of upper and lower continental crust. *Chem. Geol.* 276 (3-4), 188–197. doi:10.1016/j.chemgeo.2010.06.005

Wilson, M. (1989). *Igneous petrogenesis*. China: Springer. doi:10.1007/978-1-4020-6788-4_11

Winchester, J. A., and Floyd, P. A. (1977). Geochemical discrimination of different magma series and their differentiation products using immobile elements. *Chem. Geol.* 20, 325–343. doi:10.1016/0009-2541(77)90057-2

Wright, P., and Rodriguez, K. (2018). Reinterpreting the South atlantic pre-salt 'microbialite' reservoirs: petrographic, isotopic and seismic evidence for A shallow evaporitic lake depositional model. *First Break* 36 (5), 71–77. doi:10.3997/1365-2397.n0094

Wu, X., Guo, Q., Zhang, W., He, D., Qi, X., and Li, D. (2021). Characteristics of volcanic reservoirs and hydrocarbon accumulation of carboniferous system in junggar basin, China. *J. Earth Sci.* 32, 972–985. doi:10.1007/s12583-020-1119-y

Zalán, P. V., and Newman, E. (2019). "The fantastic microbialite reservoirs in Santos and campos basins: depositional models, crustal inheritance control on the petroleum system and risks associated for commercial discoveries," in *First EAGE workshop on pre-salt reservoir: from exploration to production* (China: European Association of Geoscientists and Engineers), 2019, 1–5. doi:10.3997/2214-4609.201982101

Zalán, P. V., Severino, M. D. C. G., Rigoti, C. A., et al. (2011). "An entirely new 3D-view of the crustal and mantle structure of A South Atlantic passive margin–santos, campos and EspÍrito santo basins, Brazil," in *AAPG annual conference and Exhibition* (USA: Expanded Abstract), 10, 13.

Zeng, G., Chen, L. H., Xu, X. S., Jiang, S. Y., and Hofmann, A. W. (2010). Carbonated mantle sources for cenozoic intra-plate alkaline basalts in shandong, north China. *Chem. Geol.* 273 (1-2), 35–45. doi:10.1016/j.chemgeo.2010.02.009